Scientific Research Publishing

Journal of High Energy Physics, Gravitation and Cosmology, 2021, 7, 1107-1156
https://www.scirp.org/journal/jhepgc
ISSN Online: 2380-4335
ISSN Print: 2380-4327

Redshift Anomaly of the 2292 MHz Radio Signal Emitted by the Pioneer-6 Space Probe as Multiple Interactions with Photo-Ionized Electrons in the Solar Corona

Alessandro Trinchera

Independent Researcher, Stuttgart, Germany
Email: trinchera.ale@gmail.com

How to cite this paper: Trinchera, A. (2021) Redshift Anomaly of the 2292 MHz Radio Signal Emitted by the Pioneer-6 Space Probe as Multiple Interactions with Photo-Ionized Electrons in the Solar Corona. *Journal of High Energy Physics, Gravitation and Cosmology*, **7**, 1107-1156.
https://doi.org/10.4236/jhepgc.2021.73066

Received: March 26, 2021
Accepted: July 11, 2021
Published: July 14, 2021

Abstract

This paper calculates the redshift of the 2292 MHz radio photon emitted by the Pioneer-6 space probe. The signal crossed the solar corona on the days close to the solar occultation between November and December 1968, the only ones for which scientific data are available, until it reached a terrestrial radio receiver. The specific study is based on a calculated orbital model of the Earth and Pioneer-6 system made on a scale of 1:100,000 by a CAD, on the New Tired Light theory adapted to the geometric and physical configuration of the topic and on a computational method. Removing the Doppler shift contributions of proper and rotational motions, due to the set-up of the receiver, and excluding the recombination factor of neutral hydrogen, which is irrelevant for distances within 1 AU, the calculation of the redshift can be traced back to the interactions between the radio signal and the electrons of the solar corona alone. The latter are contained in a Stroemgren sphere and photo-ionized by solar radiation in the UV and X-ray range. Furthermore, in order to have an interactional redshift contribution, the electrons have to satisfy the Wigner-Crystal Precondition for which their unitary potential energy is greater than their kinetic energy. Otherwise, a Thomson scattering process takes place in which the energy of the radio photon remains unchanged. The comparison between the gravitational redshift together with the interactional redshift detected from this study methodology and the total redshift obtained from other scientific studies shows a similarity between the curves, including the observational data, both in terms of values, trend of the graphs and single punctual variations.

Keywords

Redshift Anomaly, Radio Signal, Pioneer-6, Solar Corona, Plasma,

New Tired Light

1. Introduction

The phenomenon of the redshift of photons of light is measured not only at galactic level but also at extragalactic and cosmological levels. However, it is possible to measure also a local redshift component thanks to the close presence of a Star to the Earth: the Sun. This component seems to be proportional to the scale of study in the exam and the space between Sun and Earth is not experiencing any phenomenon of distancing associated with recession velocities. Once the Doppler components of orbital velocity, of proper rotation, and those relating to the gravitational field have been removed, there is always a residual redshift component. The radio signal of the Pioneer-6 space probe reaches the Earth with a characteristic peculiarity, namely its wavelength appears longer than the original one: the signal has undergone a redshift. The shift is as imperceptible as crucial in order to draw conclusions not only on the true nature of the redshift but also on its cosmological implications.

The study is based on the thesis for which the passage of the radio signal through the electron-dense solar corona causes the redshift. The theory is a development of the physics and mathematics of the New Tired Light (NTL) of the physicist L.E. Ashmore [1] [2] [3] [4] [5] who proved F. Zwicky's predictions [6] on the extragalactic redshift theorized a century ago. The study of the Pioneer-6 space probe, its orbit, and its signal, meets the physics of the English physicist adapting his mathematics to the specific problem concerning the redshift of a radio photon inside a stellar atmosphere.

Any signal that travels in the Cosmos, in the galaxy, or in the solar system undoubtedly remains unchanged under the hypothesis that space is empty. In reality, space is composed of charged particles. As we will see in detail, photo-ionized electrons assume crucial importance for the redshift. The Sun is a young star that photo-ionizes hydrogen atoms due to the radiation emitted in the UV and X-ray field, thus surrounding itself with plasma, or rather unpaired electrons and protons that permeate the stellar atmosphere and constitute the medium through which photons of light travel. Due to this fact, the electrons form the fundamental part of the Interstellar Medium (ISM). According to the mechanism that we will introduce, they first absorb the photons and then re-emit them. In this process, the re-emitted photons have lower energy as they have spent a small amount of energy to move the electrons from their equilibrium configuration. Accordingly, they show a longer wavelength or namely a redshift. On a galactic and extragalactic scale, there happens exactly the same. We can imagine areas with high density of stars that, being observed from far away, appear as astronomical objects of a punctual nature that emit radiation in the X-ray and UV fields surrounded by an atmosphere of electrons. A part is photo-ionized thus generating negative ions that permeate the galactic atmos-

pheres. Even on an extragalactic scale, the individual galaxies, made of stars, appear in turn as punctual objects that emit the same type of radiation and are surrounded by photo-ionized electrons that permeate the Intergalactic Medium (IGM).

1.1. Observational Data

The results and measurements from official scientific studies lead to further investigations. We could mention the redshift anomaly on the solar disk, made public by the study of M.G. Adam [7] and recently investigated by the author of this article [8]. The study shows that photons of light undergo a greater redshift at the limb rather than at the center of the solar disk as at the limb they travel a greater distance, valid for each orbital position, interacting with more electrons along the path. The electron density distribution has been identified in the Mex October 2006 distribution [9]. The object of study of this article is the Pioneer-6 space probe designed to orbit the Sun and to constantly emit a radio signal at a specific wavelength that passes through the solar corona and is then captured by a terrestrial receiver. Despite that, almost all Doppler tracking data, as well as all further data related to the heliocentric measurements of the space probe, are not publicly available. The Doppler data are still contained and stored on a physical device such as a magnetic coil whereas the heliocentric measurements are accessible on an online database that starts from the 80s. The latter is not very useful for calculations on the orbital mechanics of 1968, the year of our particular interest for the analysis. The only useful data available of the Pioneer-6 signal are contained in R.M. Goldstein's publication from 1969 [10]. Its purpose was to analyse the radio signal over a month in the year 1968. It was the year of the conjunction between the space probe, Sun, and Earth which in fact obscured both the space probe and the signal from a terrestrial perspective for some days. Without this very important publication, we would never have known anything about the redshift anomaly of the radio signal. Furthermore, it is important to point out that the redshift of the radio signal, originally, was not R.M. Goldstein's goal as, in reality, he wanted to study the effect of solar events on the spectral broadening of the signal. However, his study became the subject of research by a few but important subsequent studies that took place a few years later with the publications of P. Merat *et al.* [11] in 1974 and A. Accardi *et al.* [12] in 1995.

1.2. Pioneer-6 Space Probe

The Pioneer-6 space probe was launched on 1965 December 16 along an inner orbit with respect to the orbit of the Earth around the Sun. It moves in a prograde motion compared to the Earth itself. Furthermore, the orbit of the space probe is inclined by 0.1695˚ along the ecliptic plane. As its value is very small, it allows to perform the calculations of distances and orbital velocities directly as projections on the ecliptic plane with a very low margin of error. The radio frequency transmitted by Pioneer-6 is:

$$\nu_{P6} = 2292 \text{ MHz} \tag{1.1}$$

which, with c the speed of light, due to the known relation

$$c = \lambda_{P6}\nu_{P6} \tag{1.2}$$

results in a radio signal length equal to

$$\lambda_{P6} = 0.13079 \text{ m} \tag{1.3}$$

corresponding to signal energy, knowing that 1 J = 6.241509 × 10^{18} eV, calculated as

$$E_{P6} = h\nu_{P6} = 9.478 \text{ μeV} \tag{1.4}$$

The radio signal emitted by Pioneer-6 is captured by a terrestrial receiver which in orbital terms, being located on the surface of Earth, follows the orbit of the space probe in a Keplerian motion. The signal passes through the electron-dense solar corona at different distances from the Sun, farther and closer to the fictitious solar edge defined by the solar photosphere. From observational data, the measurements of the received signal, relating to the days under examination, are variably shifted towards longer wavelengths. In energy terms, we can observe how the energy of the radio signal is negligible compared to the rest mass energy of the electron:

$$E_{P6} = 9.478 \text{ μeV} \ll 511 \text{ keV} = E_{e^-} \tag{1.5}$$

thus, excluding the Compton scattering as the process responsible for the interaction between the radio signal and electrons. Moreover, this consequently excludes the blurring of the image along the trajectory. In terms of Doppler shift, the contributions connected to the radio signal emitted by the space probe differ as follows:

- Firstly, there is the contribution of the rotation of the Earth to the signal of 15 kHz/day. Secondly, there is the contribution of the difference between the orbital velocity of Earth and Pioneer-6. We can exclude these two contributions from the calculations as the receiver has been tuned continuously according to an ephemeris in order to compensate for these effects;
- Another known contribution is the increase in temperature especially when the space probe travels close to the Sun which causes a decrease in the signal frequency of about 14 Hz/day to which we have to add a measured erratic drift equal to 1.5 Hz/15min or rather 0.1 Hz/min which multiplied by 1440 min (24 h) results in 144 Hz/day. The values are variable on a daily scale. The total of the values considered coincides with a reduction of the frequency from the original signal equal to 158 Hz/day;
- Considering the only time interval under study equal to one month, corresponding only to the measurements received from R.M. Goldstein's publication, we can calculate an overall signal reduction equivalent to 4.74 kHz/month whose order of magnitude is much smaller than the nominal 2292 MHz radio signal emitted by the space probe.

As before mentioned, the only measurements received refer exactly to the time frame from 1968 November 6 to 1968 November 17 (pre-occultation phase)

and from 1968 November 29 to 1968 December 7 (post-occultation phase). Consequently, as the probe was launched in 1965, we would face, already from the first day of measurements, 1968 November 6, a reduced nominal signal of 2292 MHz-Δx kHz. It is possible to ignore this factor Δx as, first of all, the order of magnitude is negligible and furthermore the 4.74 kHz/month can be considered a worst case relative to the passage of the space probe close to the Sun in which the temperatures are at their maximum. We have not received all the other Doppler tracking data of Pioneer-6 along orbits far from the Sun in the months prior and subsequent to November and December 1968. However, we can conclude that in these time frames, where the space probe is far from the Sun, the solar temperature has a minimal impact on Pioneer-6. Additionally, the electron density of the solar corona is very low for having an impact to the interactional redshift under study.

2. Orbital Mechanics

Both Earth and Pioneer-6, having a significant difference in mass, are two astronomical objects that orbit the Sun and are therefore ruled by Keplerian laws. We restrict the observation field of the orbits to a time frame corresponding only to the values of the measurements available, or rather from 1968 November 6 to 1968 December 7. Between 1968 November 18 and 1968 November 28 there are no detections as the signal is hidden by the Sun. The most important aspect for the purposes of orbital and redshift calculations is that the measurements prior and subsequent to the solar occultation are available to us for a detailed analysis. We will use two different approaches to calculate the corresponding orbits based on the available values:

- For Earth: Kepler's orbital mechanics;
- For Pioneer-6: projection of the Sun and Pioneer-6 distances, from a terrestrial perspective, on the orbital ecliptic plane deduced from existing graphs of the heliocentric orbit.

A schematization of the two orbital models is represented in Figure 1.

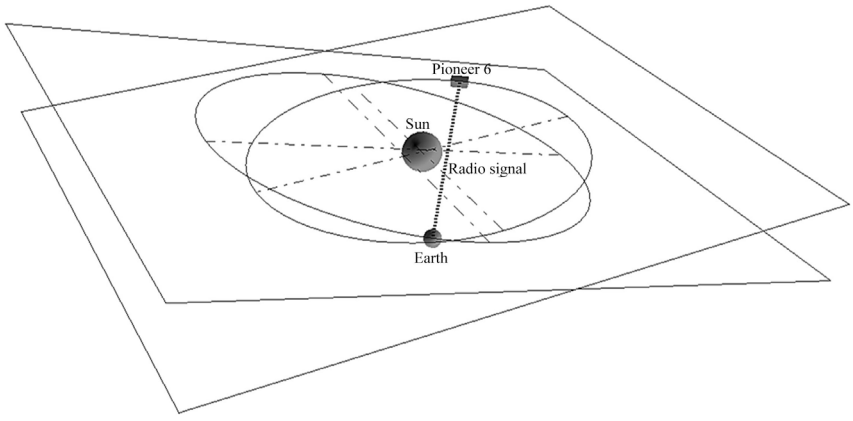

Figure 1. Schematization not on scale of the geometrical orbital model of Earth and Pioneer-6 with their orbital planes and of the radio signal on a random measurement day during pre-occultation phase.

2.1. Orbital Motion of Earth around the Sun

Kepler's equations allow us to calculate the mean anomaly which is the base value to find iteratively the eccentric anomaly *E*. We will indicate the days of measurement through the index $x = 1, 2, \cdots, 21$ which can assume only twenty-one possible values (from 1968 November 6 to 1968 December 7).

$$M_x = \frac{2\pi}{P}\left(T_x - t\right) \tag{2.1}$$

Regarding the orbital calculations, we can point out that 1968 was a leap year. All values of the formula refer to this year: T is the reference time of the measurements expressed in days from January 1, t is the perihelion passage, P is the period between two perihelion passages, R_p is the perihelion distance, R_a is the aphelion distance, e is the eccentricity:

$$e = \frac{R_a - R_p}{R_a + R_p} \tag{2.2}$$

and the semi-major axis is given by the formula

$$a = \frac{R_p}{1 - e} \tag{2.3}$$

Iteratively, we can calculate the eccentric anomaly E as:

$$E_x - e\sin\left(E_x\right) = M_x \tag{2.4}$$

Once the equality has been verified by iterations, we can determine the exact linear and angular position of the Earth in the orbit respectively as:

$$d_x = a\left(1 - e\cos E_x\right) \tag{2.5}$$

and

$$\phi_x = 2\tan^{-1}\left(\sqrt{\frac{1+e}{1-e}} \cdot \tan\frac{E_x}{2}\right) \tag{2.6}$$

The orbital velocity expressed in Km/sec is

$$v_{orb_x} = \sqrt{G\left(M_s + M_E\right)\left(\frac{2}{d_x} - \frac{1}{a}\right)} \tag{2.7}$$

All given and calculated start parameters are enclosed in Table 1 whereas the calculated orbital parameter of Earth during pre-occultation and post-occultation phase in the year 1968 are shown in Table 2.

Table 1. Given and calculated start orbital parameter of Earth in the year 1968.

P	t	R_p	R_p	R_a	R_a	e	a	M_S	M_E
[days]	[days]	[AU]	[m]	[AU]	[m]	[-]	[m]	[kg]	[Kg]
367.51	4	0.98329	1.47098E+11	0.01673	1.521E+11	0.0167	1.49599E+11	1.989E+30	5.972E+24

Table 2. Orbital parameter of Earth during pre-occultation and post-occultation phase in the year 1968.

Parameters																								
		Pre-occultation phase															Post-occultation phase								
v_{orbx}	Φ_x	d_x	E_x	E_x	M_x	T_x	x	date																
[Km/s]	[deg]	[m]	[deg]	[rad]	[rad]	[day]	[indexed day]	[calender day]																
30.04	−60.94	1.48353E+11	299.89	5.23	5.25	311	1	Nov 06, 1968																
30.05	−59.94	1.48315E+11	300.88	5.25	5.27	312	2	Nov 07, 1968																
30.05	−58.95	1.48279E+11	301.87	5.27	5.28	313	3	Nov 08, 1968																
30.06	−57.95	1.48242E+11	302.86	5.29	5.30	314	4	Nov 09, 1968																
30.07	−56.95	1.48206E+11	303.85	5.30	5.32	315	5	Nov 10, 1968																
30.07	−56.00	1.48172E+11	304.80	5.32	5.33	316	6	Nov 11, 1968																
30.08	−54.95	1.48135E+11	305.83	5.34	5.35	317	7	Nov 12, 1968																
30.09	−53.95	1.481E+11	306.82	5.36	5.37	318	8	Nov 13, 1968																
30.10	−52.95	1.48066E+11	307.81	5.37	5.39	319	9	Nov 14, 1968																
30.10	−51.95	1.48032E+11	308.80	5.39	5.40	320	10	Nov 15, 1968																
30.11	−50.94	1.47998E+11	309.80	5.41	5.42	321	11	Nov 16, 1968																
30.12	−49.95	1.47966E+11	310.78	5.42	5.44	322	12	Nov 17, 1968																
30.19	−37.91	1.4761E+11	322.67	5.63	5.64	334	13	Nov 29, 1968																
30.19	−36.91	1.47584E+11	323.66	5.65	5.66	335	14	Nov 30, 1968																
30.20	−35.86	1.47558E+11	324.70	5.67	5.68	336	15	Dec 01, 1968																
30.20	−34.87	1.47534E+11	325.67	5.68	5.69	337	16	Dec 02, 1968																
30.21	−33.88	1.4751E+11	326.65	5.70	5.71	338	17	Dec 03, 1968																
30.21	−32.88	1.47486E+11	327.64	5.72	5.73	339	18	Dec 04, 1968																
30.22	−31.85	1.47463E+11	328.65	5.74	5.74	340	19	Dec 05, 1968																
30.22	−30.86	1.47441E+11	329.63	5.75	5.76	341	20	Dec 06, 1968																
30.23	−29.85	1.4742E+11	330.62	5.77	5.78	342	21	Dec 07, 1968																

Following the calculations, we can trace the exact position of Earth during the phases prior and subsequent to the solar occultation as shown in **Figure 2**. The orbital schematization is deliberately exaggerated towards an elliptical shape to bring out the orbital parameters more prominently.

2.2. Orbital Motion of Pioneer-6 around the Sun

The orbit tracking the Pioneer-6 space probe is very complex as there are no orbital data in the year of analysis 1968 in the official databases. There are uncertainties related to the exact orbital period, which, as known, is not constant over the years, but characterized by a change in the passage to the perihelion from year to year. However, it was possible to determine the exact position of the perihelion by referring to the image of the heliocentric orbit projected on the ecliptic plane [13]. The pixel value corresponding to 1 AU was determined on scale. By definition of perihelion, as the point of passage of the space probe closest to the Sun, it is located exactly on the semi-major axis of the Earth orbit but on the opposite side. As a matter of fact, the position of perihelion and aphelion in the orbit of Pioneer-6 is reversed to their position in the orbit of the Earth. Obviously,

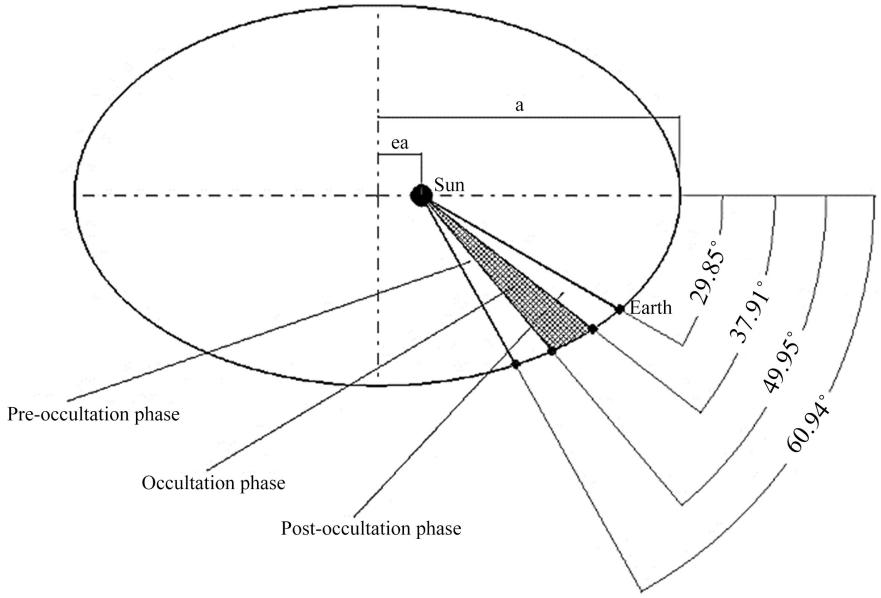

Figure 2. Schematization of Earth orbital position around the Sun during pre-occultation and post-occultation phase based on the calculations.

the corresponding values differ. The orbital rotation of the space probe and Earth are in agreement in an anti-clockwise direction due to the shape of the heliocentric orbits projected on the ecliptic plane.

The reasons stated at the beginning of the paragraph are sufficient elements for not proceeding with the direct calculation of the Pioneer-6 orbit. However, by knowing both the orbital position of Earth on each measurement day and the distance of the space probe from the Sun, observed from a terrestrial perspective [14], we are able to trace the exact position of the space probe through projections in the ecliptic plane. By observing the edge-on orbits at the ecliptic plane level, the orbit of Pioneer-6 is inclined by 0.1695˚ with respect to the orbit of Earth. Therefore, knowing the distance between Sun and Earth from Kepler's equations, we can determine graphically the distance between Sun and Pioneer-6 for each orbital position. In turn, we can calculate the angles and by the same Keplerian approach, we can thus obtain the orbital velocities of the space probe. It is important to point out that the latter, particularly the difference in orbital speeds between Earth and Pioneer-6, do not provide any useful contribution to the interactional redshift as they have already been neglected previously due to the fact that the receiver has been tuned according to an ephemeris in order to compensate for these redshift components. The values of the orbital velocities have been left in the tables in order to allow other researchers to verify the calculations in further studies. We have to distinguish between:

- Pre-occultation phase: in which, from the point of view of a terrestrial observer, the signal of the Pioneer-6 space probe appears to the right-hand side of the Sun until the last day of signal reception (1968 November 17) before disappearing in the occultation phase;
- Post-occultation phase: in which, from the point of view of a terrestrial ob-

server, the signal of the Pioneer-6 space probe appears to the left-hand side of the Sun starting from the first post-occultation day (1968 November 29).

In Figure 3 and Figure 4, it is possible to visualize the orbital models of the Earth-Pioneer-6 system in the pre-occultation and post-occultation phase. As one can observe, the orbits tend exaggeratedly towards an elliptical shape in order to highlight all the orbital parameters in a better way. In reality, as the eccentricity is a small value, the orbits are almost circular.

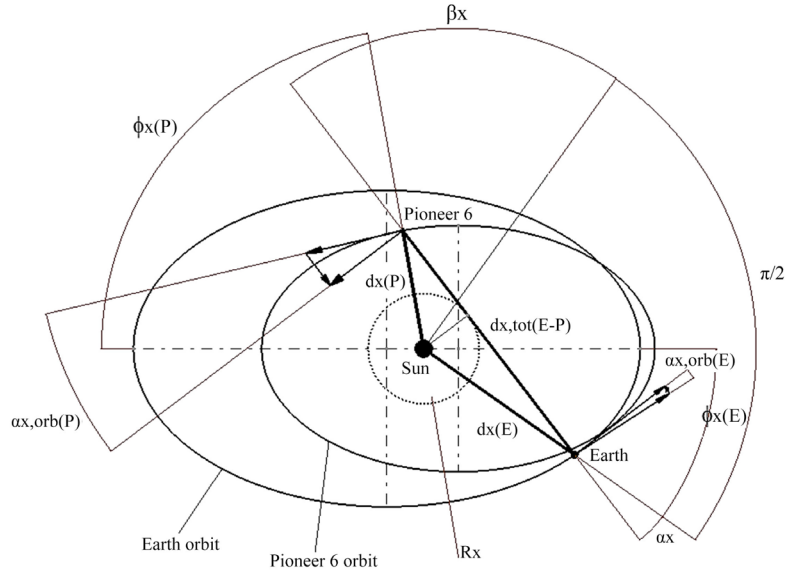

(a)

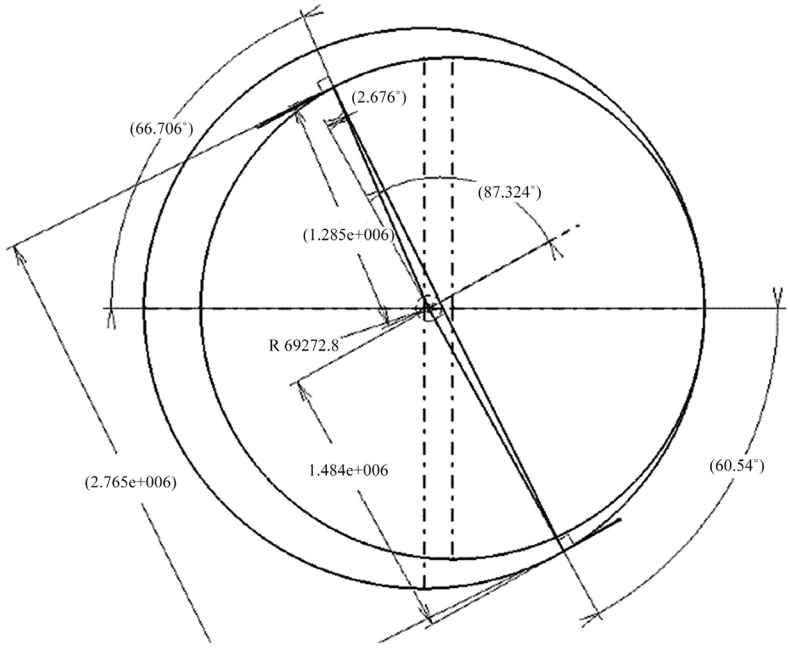

(b)

Figure 3. Schematization not on scale (a) and a real representation on scale (b) of the orbital model Earth-Pioneer-6 on a generic day x in pre-occultation phase (from 1968 November 6 to 1968 November 17).

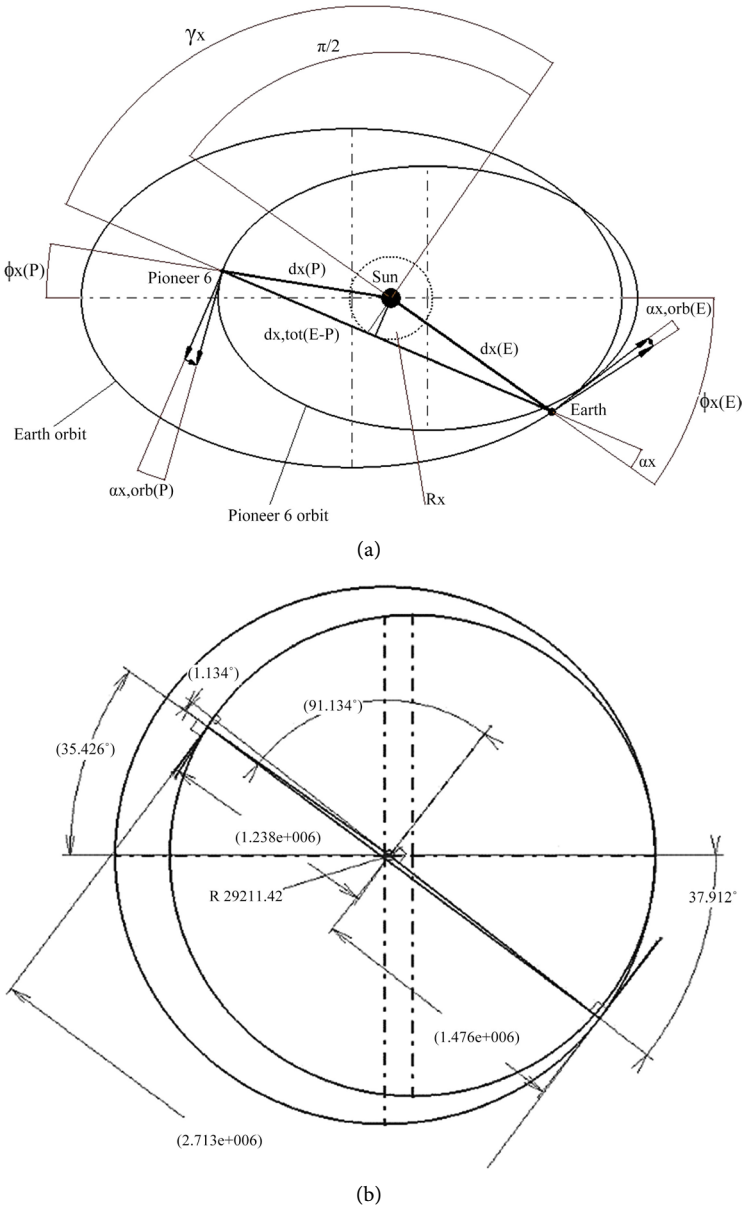

Figure 4. Schematization not on scale (a) and a real representation on scale (b) of the orbital model Earth-Pioneer-6 on a generic day x in post-occultation phase (from 1968 November 29 to 1968 December 7).

Once the orbital model has been set up in the Computer Aided Design (CAD) and scaled to 1:100,000 (which is the reason why the distances differ in order of magnitude, whereas the angles are unchanged), we can set the following calculation procedure in the spreadsheet: 1) set $\Phi_x(E)$; 2) set the radius R_x; 3) measure all the orbital parameters of the Pioneer-6 space probe; 4) calculate the parameters q_x (corresponding to the $d_x(E)$) and m_x (angular coefficient of the straight line travelled by the radio signal). All given and calculated start parameters are enclosed in **Table 3** whereas the orbital parameter of Pioneer-6 during pre-occultation and post-occultation phase are shown in **Table 4** (in the table the suffix E stands for Earth and P for Pioneer-6).

Table 3. Given and deduced orbital parameter of Pioneer-6 in the year 1968.

P	t	R_p	R_p	R_a	R_a	e	a	M_S	M_{P6}
[days]	[days]	[AU]	[m]	[AU]	[m]	[-]	[m]	[kg]	[Kg]
310.3	49.4	0.814	1.21772E+11	0.985	1.47353E+11	0.0951	1.34563E+11	1.989E+30	64

Table 4. Orbital parameter of Pioneer-6 during pre-occultation and post-occultation phase deduced from orbital parameter of Earth in the year 1968. E: Earth, P: Pioneer-6.

Parameters																							
Pre-occultation phase														Post-occultation phase									
m_x	β_x	α_x	$\Phi_x(P)$	$d_x(P)$	$d_{x,tot}(EP)$	R_x	$r_{t,x}$	$\Phi_x(E)$	$d_x(E) = q_x$	x	date												
[–]	[deg]	[deg]	[deg]	[m]	[m]	[m]	[R_S]	[deg]	[m]	[indexed day]	[calenderday]												
21.395	87.324	2.676	−66.706	1.285E+11	2.765E+11	6.92728E+09	9.96	−60.940	1.48353E+11	1	Nov 06, 1968												
22.904	87.500	2.500	−65.334	1.283E+11	2.763E+11	6.46824E+09	9.30	−59.944	1.48315E+11	2	Nov 07, 1968												
24.264	87.640	2.360	−64.043	1.28E+11	2.76E+11	6.10658E+09	8.78	−58.949	1.48279E+11	3	Nov 08, 1968												
25.936	87.792	2.208	−62.718	1.278E+11	2.758E+11	5.71014E+09	8.21	−57.949	1.48242E+11	4	Nov 09, 1968												
28.352	87.980	2.020	−61.318	1.275E+11	2.755E+11	5.22328E+09	7.51	−56.951	1.48206E+11	5	Nov 10, 1968												
30.369	88.114	1.886	−60.077	1.273E+11	2.753E+11	4.87553E+09	7.01	−55.995	1.48172E+11	6	Nov 11, 1968												
33.321	88.281	1.719	−58.677	1.271E+11	2.751E+11	4.44431E+09	6.39	−54.953	1.48135E+11	7	Nov 12, 1968												
36.956	88.450	1.550	−57.331	1.268E+11	2.748E+11	4.00614E+09	5.76	−53.951	1.481E+11	8	Nov 13, 1968												
41.242	88.611	1.389	−55.964	1.266E+11	2.746E+11	3.58883E+09	5.16	−52.951	1.48066E+11	9	Nov 14, 1968												
46.880	88.778	1.222	−54.609	1.264E+11	2.743E+11	3.15762E+09	4.54	−51.955	1.48032E+11	10	Nov 15, 1968												
53.045	88.920	1.080	−53.282	1.262E+11	2.741E+11	2.78900E+09	4.01	−50.936	1.47998E+11	11	Nov 16, 1968												
69.953	89.181	0.819	−51.732	1.259E+11	2.739E+11	2.11435E+09	3.04	−49.951	1.47966E+11	12	Nov 17, 1968												
−50.519	91.134	1.312	−35.426	1.238E+11	2.713E+11	2.92114E+09	−4.20	−37.912	1.4761E+11	13	Nov 29, 1968												
−43.663	91.312	1.483	−34.028	1.236E+11	2.711E+11	3.38018E+09	−4.86	−36.907	1.47584E+11	14	Nov 30, 1968												
−38.626	91.483	1.637	−32.601	1.235E+11	2.709E+11	3.81835E+09	−5.49	−35.856	1.47558E+11	15	Dec 01, 1968												
−34.991	91.637	1.816	−31.279	1.233E+11	2.707E+11	4.21479E+09	−6.06	−34.875	1.47534E+11	16	Dec 02, 1968												
−31.540	91.816	1.97	−29.891	1.232E+11	2.705E+11	4.67383E+09	−6.72	−33.881	1.4751E+11	17	Dec 03, 1968												
−29.073	91.970	2.157	−28.545	1.231E+11	2.704E+11	5.07027E+09	−7.29	−32.876	1.47486E+11	18	Dec 04, 1968												
−26.550	92.157	2.338	−27.103	1.229E+11	2.702E+11	5.55017E+09	−7.98	−31.848	1.47463E+11	19	Dec 05, 1968												
−24.493	92.338	2.512	−25.714	1.228E+11	2.7E+11	6.01616E+09	−8.65	−30.860	1.47441E+11	20	Dec 06, 1968												
−22.794	92.512	1.312	−24.324	1.227E+11	2.698E+11	6.46129E+09	−9.29	−29.854	1.4742E+11	21	Dec 07, 1968												

Continued

Total approach comp. $v_{x,orb}$(E-P)	Approach comp. $v_{x,orb}$(P)	$v_{x,orb}$(P)	α_{orb}(P)	Approach comp. $v_{x,orb}$(E)	$v_{x,orb}$(E)	α_{orb}(E)
[m/sec]	[m/sec]	[m/sec]	[deg]	[m/sec]	[m/sec]	[deg]
2824.25	987.35	32,857.020	1.722	1836.89	30,037.624	3.506
2810.34	1069.83	32,943.406	1.861	1740.51	30,045.098	3.321
2789.62	1126.18	32,944.406	1.959	1663.43	30,052.485	3.173
2768.40	1189.43	32,945.406	2.069	1578.97	30,059.825	3.011
2748.89	1272.78	32,946.406	2.214	1476.11	30,067.076	2.814
2726.53	1324.54	32,947.406	2.304	1402.00	30,073.936	2.672
2701.88	1392.38	32,948.406	2.422	1309.51	30,081.327	2.495
2677.83	1461.94	32,949.406	2.543	1215.89	30,088.347	2.316
2652.75	1526.33	32,950.406	2.655	1126.42	30,095.266	2.145
2626.75	1593.01	32,951.406	2.771	1033.74	30,102.059	1.968
2597.23	1643.61	32,952.406	2.859	953.62	30,108.916	1.815
2576.35	1765.43	32,953.406	3.071	810.92	30,115.445	1.543
2168.10	2459.98	32,954.406	4.281	−291.88	30,187.066	−0.554
2130.57	2523.15	32,955.406	4.391	−392.57	30,192.305	−0.745
2088.72	2578.85	32,956.406	4.488	−490.13	30,197.650	−0.93
2049.44	2627.67	32,957.406	4.573	−578.23	30,202.523	−1.097
2009.62	2689.67	32,958.406	4.681	−680.05	30,207.333	−1.29
1968.04	2736.76	32,959.406	4.763	−768.72	30,212.075	−1.458
1926.24	2801.05	32,960.406	4.875	−874.81	30,216.794	−1.659
1885.34	2863.61	32,961.406	4.984	−978.27	30,221.201	−1.855
1842.90	2920.43	32,962.406	5.083	−1077.53	30,225.556	−2.043

From the geometry of the orbits, we can calculate the total distance between Earth and Pioneer-6, either in the pre-occultation or in the post-occultation phase, as shown in the following formula:

$$d_{x_{tot}}(EP)=\sqrt{\left[d_x(P)\cdot\sin\phi_x(P)+d_x(E)\cdot\sin\phi_x(E)\right]^2+\left[d_x(P)\cdot\cos\phi_x(P)+d_x(E)\cdot\cos\phi_x(E)\right]^2} \quad (2.8)$$

The trend of the total distance over the measurement days is shown in **Figure 5**.

From the values determined in the tables, we can draw important considerations:

- The total distance between Earth and Pioneer-6, $d_{x,tot}(EP)$, decreases passing from the pre-occultation to the post-occultation phase, in accordance with the heliocentric orbit projected on the ecliptic plane in 1968. By measuring the distances from the heliocentric orbit (which has fixed the position of Earth and Sun in the diagram), it is possible to calculate small deviations in the values of the distances. The latter has to be attributed to the fact that this last graph [13], differently to our analytical calculations conducted, is a graphical approximation. The Earth is actually in motion and varies the or-

bital distances not remaining fixed on a constant distant orbit equal to 1 AU;

- The difference between the orbital velocity components of Pioneer-6 and Earth gives an approaching contribution along the terrestrial observation line in the pre-occultation phase, whereas the orbital velocity components of the Earth in the post-occultation phase change sign, from negative to positive, giving a receding contribution.

The orbital models on the scale of Earth and Pioneer-6 during pre-occultation and post-occultation phase, extracted from the CAD, are listed in Table 5.

Similarly, as previously shown with the orbit of the Earth, we can trace the exact position of the Pioneer-6 space probe during the pre-occultation and post-occultation phase according to Figure 6. In this figure, the excessive elliptical form is as well a schematization.

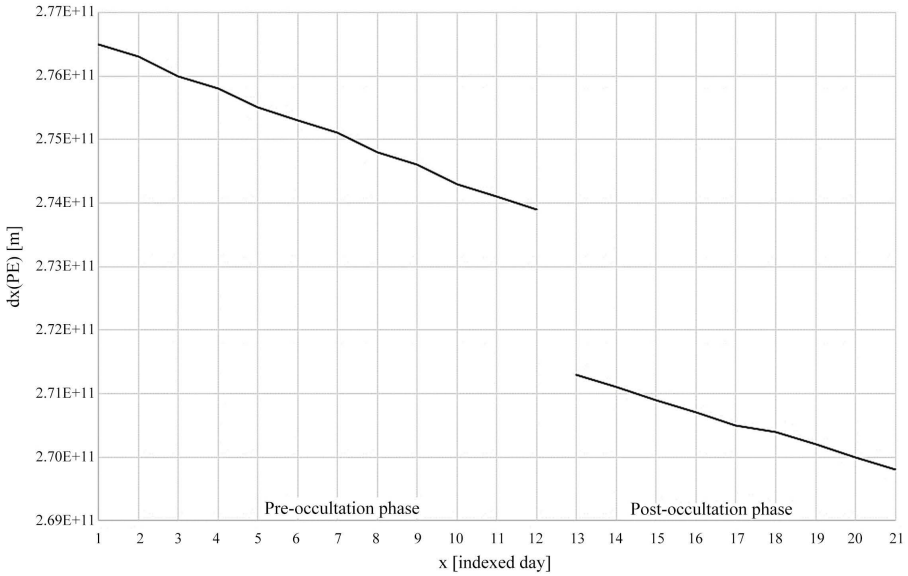

Figure 5. Total distance between Earth and Pioneer-6 over all measurement days.

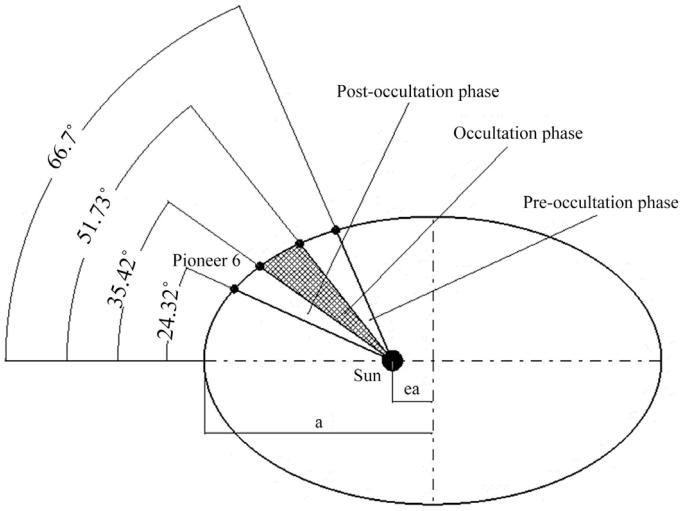

Figure 6. Schematization of the Pioneer-6 orbital position around the Sun during pre-occultation and post-occultation phase.

Table 5. Orbital parameter of Earth and Pioneer-6 from Nov 6, 1968 to Nov 17, 1968 and from Nov 19, 1968 to Dec 6, 1968 extracted from the orbital geometrical model on scale.

Nov 6, 1968 (pre-occultation)	Nov 7, 1968 (pre-occultation)	Nov 8, 1968 (pre-occultation)
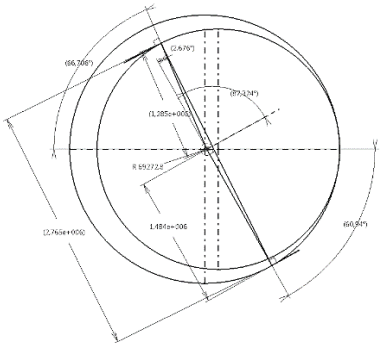	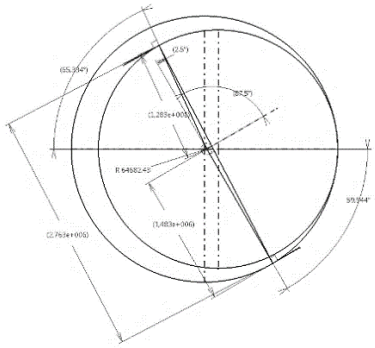	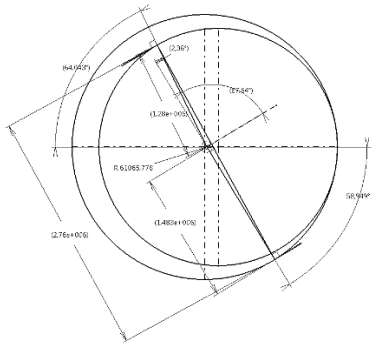
Nov 9, 1968 (pre-occultation)	Nov 10, 1968 (pre-occultation)	Nov 11, 1968 (pre-occultation)
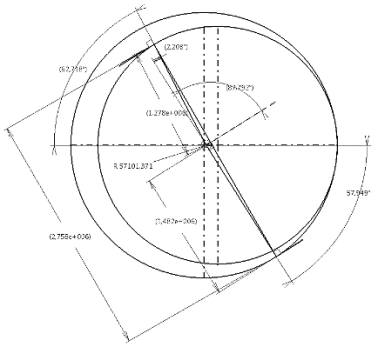	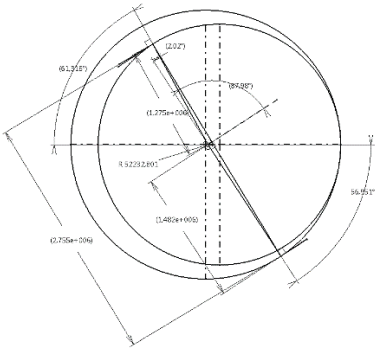	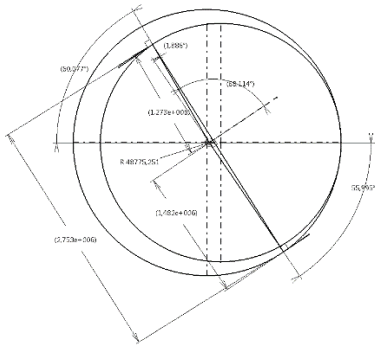
Nov 12, 1968 (pre-occultation)	Nov 13, 1968 (pre-occultation)	Nov 14, 1968 (pre-occultation)
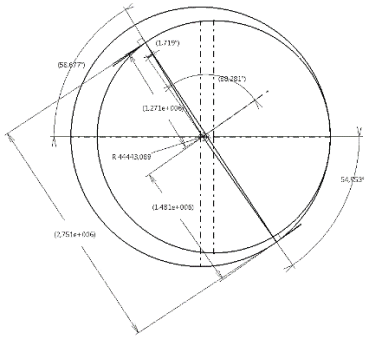	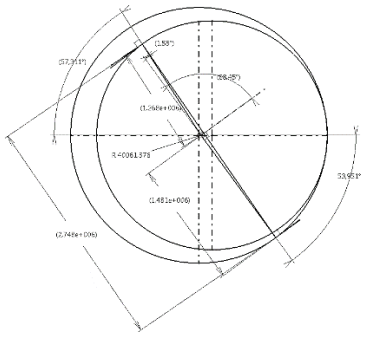	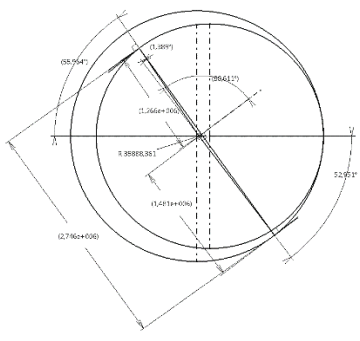
Nov 15, 1968 (pre-occultation)	Nov 16, 1968 (pre-occultation)	Nov 17, 1968 (pre-occultation)
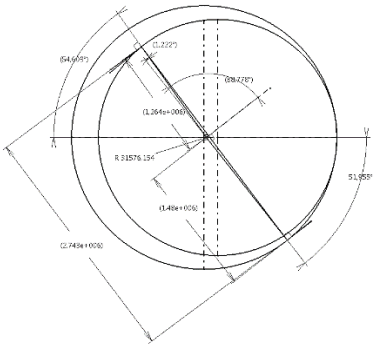	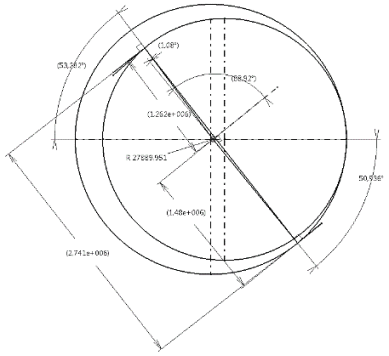	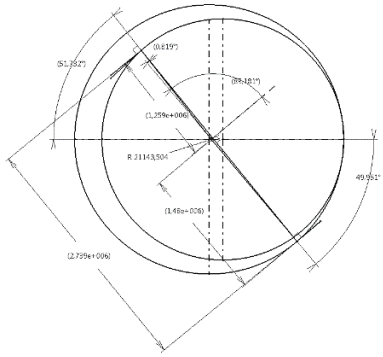

Continued

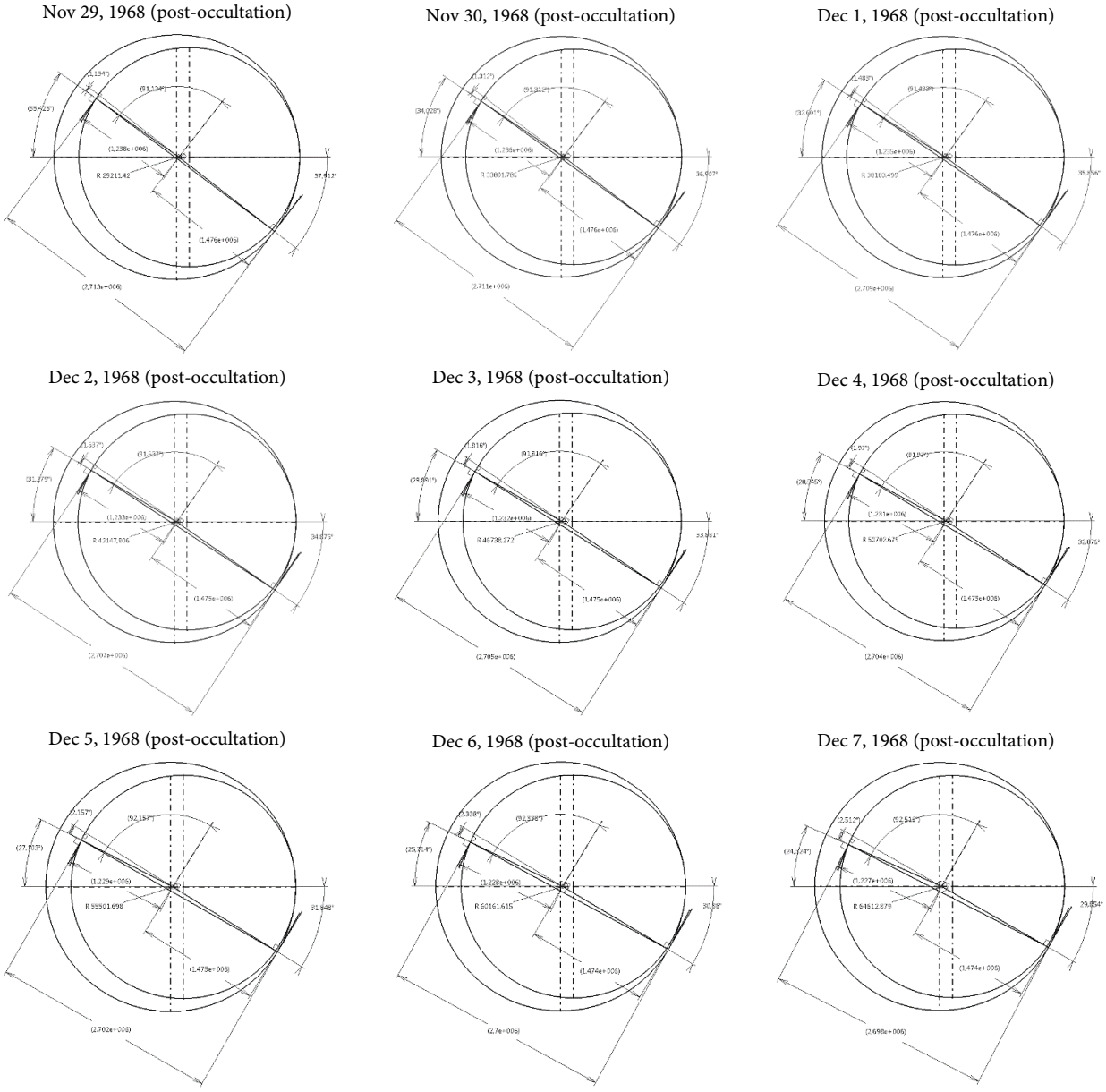

The distance R_x from the Sun expressed in meters, or $r_{t,x}$ expressed in solar radii, observationally measured, is orthogonal to the direction of a terrestrial observer's view. Due to this fact, starting from the known values R_x and q_x (where q_x corresponds to the distance between Sun and Earth or rather $d_x(E)$) of a generic day of measurement x, we are able to determine, alternatively to the direct measurements on the CAD, all the angles α_x, β_x and γ_x of the triangles in the pre-occultation and post-occultation phase. With these angles, we can draw the straight line on the graph representing the path crossed by the radio signal. In Figure 7, we can visualize the path of the radio signal with respect to the reference system centered into the Sun and rotated, for simplicity, so that the distance q_x is vertical.

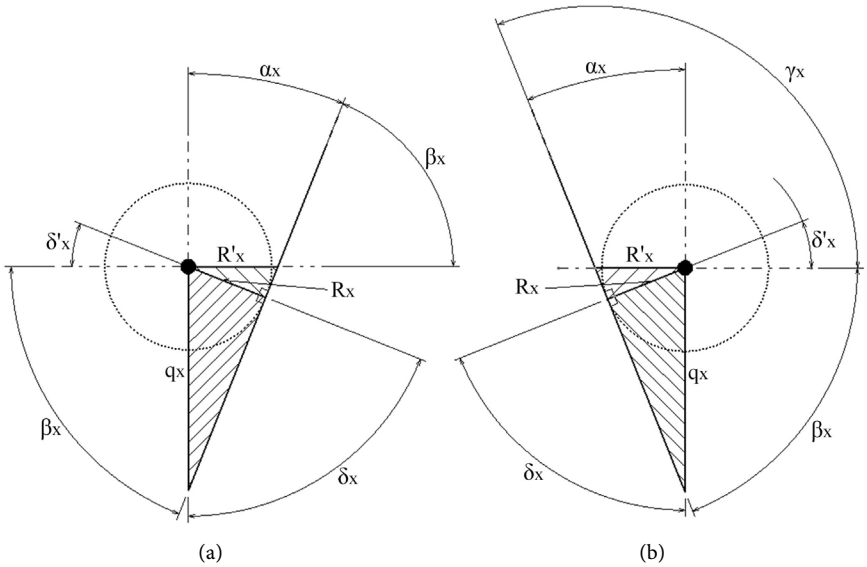

Figure 7. Schematization of the radio signal path on a generic measurement day in pre-occultation phase (a) and in post-occultation phase (b).

From the first triangle,

$$\delta_x + 90 + \alpha_x = 180 \tag{2.9}$$

$$\delta_x = 90 - \alpha_x \tag{2.10}$$

Moreover, we can calculate that:

$$\delta_x + \delta_x' = 90 \tag{2.11}$$

$$90 - \alpha_x + \delta_x' = 90 \tag{2.12}$$

$$\delta_x' = \alpha_x \tag{2.13}$$

From the smallest triangle, we can write the following expression

$$R_x' \sin\beta_x = R_x \tag{2.14}$$

From the larger triangle, we can prove that:

$$180 = \beta_x + \alpha_x + 90 \tag{2.15}$$

$$\beta_x = 90 - \alpha_x \tag{2.16}$$

and

$$\frac{R_x'}{q_x} = \tan\alpha_x \tag{2.17}$$

$$\frac{R_x}{q_x \sin\beta_x} = \tan\alpha_x \tag{2.18}$$

$$\frac{R_x}{q_x \sin\left(90 - \alpha_x\right)} = \tan\alpha_x \tag{2.19}$$

$$\frac{R_x}{q_x \cos\alpha_x} = \tan\alpha_x \tag{2.20}$$

$$\frac{R_x}{q_x \cos\alpha_x} = \frac{\sin\alpha_x}{\cos\alpha_x} \tag{2.21}$$

$$\alpha_x = \sin^{-1}\left(\frac{R_x}{q_x}\right) \tag{2.22}$$

Taking into consideration the smallest triangle again, we can also calculate that

$$180 = \beta_x + \delta'_x + 90 \tag{2.23}$$

$$180 = \beta_x + \alpha_x + 90 \tag{2.24}$$

$$\beta_x = 90 - \alpha_x \tag{2.25}$$

from which, in the pre-occultation phase, the angular coefficient can be calculated as:

$$m_x = \tan\beta_x > 0 \tag{2.26}$$

In the post-occult phase, we determine that:

$$180 = \beta_x + \gamma_x \tag{2.27}$$

$$\gamma_x = 180 - \beta_x \tag{2.28}$$

$$\gamma_x = 180 - 90 + \alpha_x \tag{2.29}$$

$$\gamma_x = 90 + \alpha_x \tag{2.30}$$

It allows us to determine the angular coefficient of the line as:

$$m_x = \tan\gamma_x < 0 \tag{2.31}$$

All previously determined values correspond exactly to those measured by the CAD.

3. Electron Distribution in the Solar Corona

As observed in a previous study [8], the electron density in the solar corona that better approximates the real trend expressed in el/m^3 is the following:

$$n_e = \begin{cases} 0 & \text{for } r < 1 \\ \dfrac{t}{r^{\varepsilon}} & \text{for } 1 \le r \le \dfrac{d_{x,E} - R_E}{R_s} \text{ and } 1 \le r \le \dfrac{d_{x,P}}{R_s} \end{cases} \tag{3.1}$$

where

$$t = p \cdot 10^{12} \tag{3.2}$$

is a numerical coefficient and 10^{12} is the conversion factor to express the electron density in el/m^3. The coefficient

$$p = 1.90 \tag{3.3}$$

is a dimensionless numerical parameter of the solar corona. In the initial formula, r is the solar radius expressed in solar radii and ε is the numerical dimensionless fall-off parameter of the curve as result of the same experimental observations, equal to

$$\varepsilon = 1.54 \tag{3.4}$$

Figure 8 schematizes the electron distribution with respect to the Sun and two generic radio signals emitted during two generic measurement days in the pre-occultation phase.

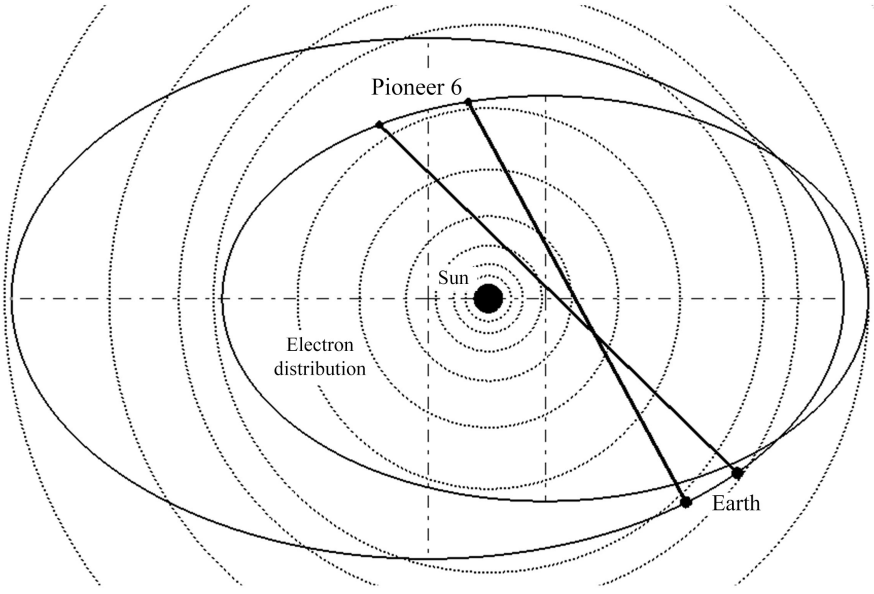

Figure 8. Schematization not on scale of the variable electron densities (concentric circles) decreasing from the photosphere of the Sun to higher radii during two generic measurement days in the pre-occultation phase.

The electron density extends up to Earth and Pioneer-6 varying from a very high value close to the photosphere to lower values close to, respectively, Earth and Pioneer-6. For simplicity, we have chosen the mathematical distribution which has only one contribution of decreasing power as fall-off parameter that well approximates the real trend of the electrons in the solar corona. This allows us to avoid equations with big orders which might complicate the calculations and making its computing time quite longer. The curve of the electron density, cut for high radii in order to be able to focus on the curve variation, is summarized in **Figure 9**.

The re-combination factor, which moves the electrons back into the neutral hydrogen atom, is not taken into account as it is negligible, equal to 0.95, within 1 AU [15]. So, considering all the involved astrophysical parameters and once understood the geometric configuration of the problem, we can proceed with the first steps which will lead us to calculate the redshift in the next paragraphs. Firstly, it is necessary to calculate the electron density for each radius of the solar corona along the path which terminates at the orbital position of Earth and Pioneer-6. We set an increment in the radii equal to the increment factor χ in order to study the signal and, accordingly, the redshift at its best resolution. The average value of electrons expressed in el/m^3 in a generic interval in the upper part of the orbital model, in which we have a decreasing exponential trend, is calculated as follows:

$$\overline{n}_e = \frac{\int_{r_{i-1}}^{r_{i-\chi}} \frac{t}{r^{\varepsilon}} \mathrm{d}r}{\left(r_{i-\chi} - r_{i-1}\right)} \tag{3.5}$$

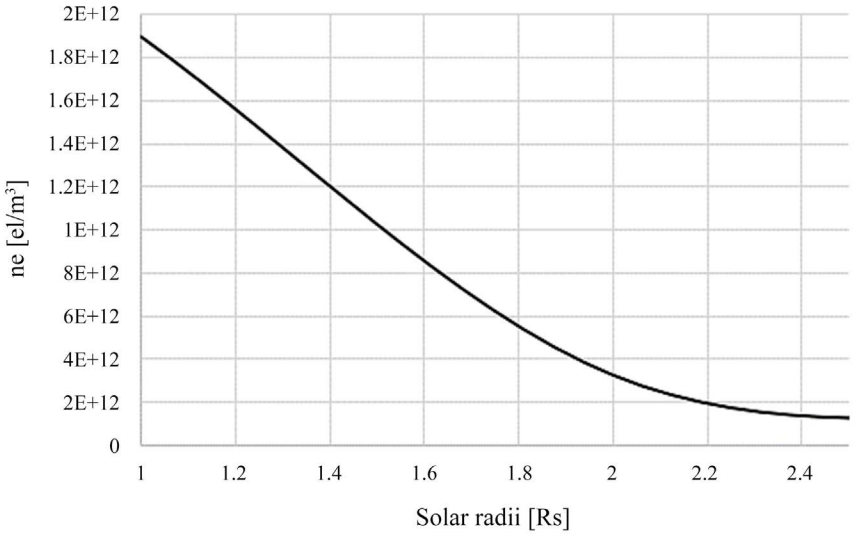

Figure 9. Distribution of electrons in the solar corona according to Mex October 2006.

$$\overline{n}_e = \frac{t}{\left(r_{i-\chi} - r_{i-1}\right)} \int_{r_{i-1}}^{r_{i-\chi}} r^{-\varepsilon} \mathrm{d}r \tag{3.6}$$

$$\overline{n}_e = \frac{t}{\left(r_{i-\chi} - r_{i-1}\right)} \left[\frac{r^{1-\varepsilon}}{1-\varepsilon}\right]_{r_{i-1}}^{r_{i-\chi}} \tag{3.7}$$

$$\overline{n}_e = \frac{t}{(1-\varepsilon)\left(r_{i-\chi} - r_{i-1}\right)} \left(r_{i-\chi}^{1-\varepsilon} - r_{i-1}^{1-\varepsilon}\right) \tag{3.8}$$

Only at the very first calculation step, at the emission of the radio signal, the following condition has to be valid as there has not yet been assigned any increase

$$r_{i-\chi} = r_i \tag{3.9}$$

The average value of electrons expressed in el/m^3 in a generic interval in the lower part of the orbital model, in which we have decreasing exponential trend, is calculated as follows:

$$\overline{n}_e = \frac{\int_{r_{i+\chi}}^{r_{i+1}} \frac{t}{r^{\varepsilon}} \mathrm{d}r}{\left(r_{i+1} - r_{i+\chi}\right)} \tag{3.10}$$

$$\overline{n}_e = \frac{t}{\left(r_{i+1} - r_{i+\chi}\right)} \int_{r_{i+\chi}}^{r_{i+1}} r^{-\varepsilon} \mathrm{d}r \tag{3.11}$$

$$\overline{n}_e = \frac{t}{\left(r_{i+1} - r_{i+\chi}\right)} \left[\frac{r^{1-\varepsilon}}{1-\varepsilon}\right]_{r_{i+\chi}}^{r_{i+1}} \tag{3.12}$$

$$\overline{n}_e = \frac{t}{(1-\varepsilon)\left(r_{i+1} - r_{i+\chi}\right)} \left(r_{i+1}^{1-\varepsilon} - r_{i+\chi}^{1-\varepsilon}\right) \tag{3.13}$$

Similarly to the previous remark, the following condition has to be valid at the very first calculation step

$$r_{i+\chi} = r_i \tag{3.14}$$

In Figure 10, it is possible to visualize the trend of the average density along different solar radii.

An essential condition necessary for the success of the calculation is that the physical interval, expressed in solar radii, has to be greater than or equal to the mean free path Λ, taking into account an average-electron density. In this way, we can calculate how long a physical interval has to be in order to detect, on average, at least one interaction between the radio signal and an electron. For the upper part of the orbital model, we can calculate the next interval as:

$$I_{physic} = \Lambda \tag{3.15}$$

$$\left(r_{i-\chi} - r_{i-1}\right) R_s = \frac{1}{2 r_e \lambda \overline{n}_e} \tag{3.16}$$

$$\left(r_{i-\chi} - r_{i-1}\right) R_s = \frac{1}{2 r_e \lambda \dfrac{t}{(1-\varepsilon)\left(r_{i-\chi} - r_{i-1}\right)} \left(r_{i-\chi}^{1-\varepsilon} - r_{i-1}^{1-\varepsilon}\right)} \tag{3.17}$$

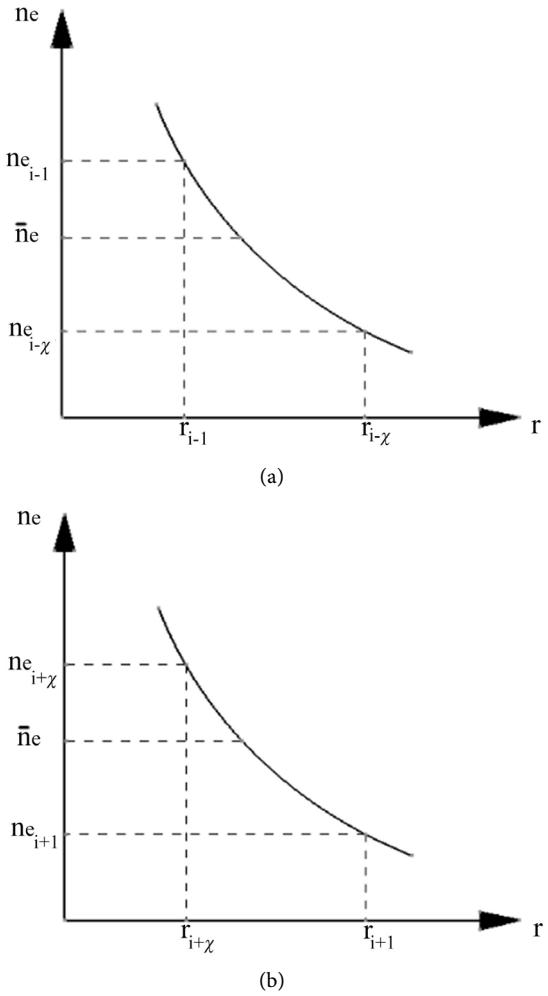

Figure 10. Average value of a physical interval in the upper part (a) and in the lower part (b) of the orbital model.

$$\left(r_{i-\chi}-r_{i-1}\right)R_s=\frac{(1-\varepsilon)\left(r_{i-\chi}-r_{i-1}\right)}{k\left(r_{i-\chi}^{1-\varepsilon}-r_{i-1}^{1-\varepsilon}\right)} \tag{3.18}$$

$$k\left(r_{i-\chi}^{1-\varepsilon}-r_{i-1}^{1-\varepsilon}\right)R_s=1-\varepsilon \tag{3.19}$$

$$kR_s r_{i-\chi}^{1-\varepsilon}-kR_s r_{i-1}^{1-\varepsilon}=1-\varepsilon \tag{3.20}$$

$$r_{i-1}=\sqrt[\frac{1}{1-\varepsilon}]{r_{i-\chi}^{1-\varepsilon}-\frac{1-\varepsilon}{kR_s}} \tag{3.21}$$

whereas for the lower part of the orbital model, we can instead calculate the next interval as:

$$I_{physic}=\Lambda \tag{3.22}$$

$$\left(r_{i+1}-r_{i+\chi}\right)R_s=\frac{1}{2r_e\lambda\overline{n}_e} \tag{3.23}$$

$$\left(r_{i+1}-r_{i+\chi}\right)R_s=\frac{1}{2r_e\lambda\dfrac{t}{(1-\varepsilon)\left(r_{i+1}-r_{i+\chi}\right)}\left(r_{i+1}^{1-\varepsilon}-r_{i+\chi}^{1-\varepsilon}\right)} \tag{3.24}$$

$$\left(r_{i+1}-r_i\right)R_s=\frac{(1-\varepsilon)\left(r_{i+1}-r_{i+\chi}\right)}{k\left(r_{i+1}^{1-\varepsilon}-r_{i+\chi}^{1-\varepsilon}\right)} \tag{3.25}$$

$$k\left(r_{i+1}^{1-\varepsilon}-r_{i+\chi}^{1-\varepsilon}\right)R_s=1-\varepsilon \tag{3.26}$$

$$kR_s r_{i+1}^{1-\varepsilon}-kR_s r_{i+\chi}^{1-\varepsilon}=1-\varepsilon \tag{3.27}$$

$$r_{i+1}=\sqrt[\frac{1}{1-\varepsilon}]{r_{i+\chi}^{1-\varepsilon}+\frac{1-\varepsilon}{kR_s}} \tag{3.28}$$

After Equation (3.17) and Equation (3.24), we have defined the factor k as the product of twice the classic electron radius with the radio wavelength under examination, multiplied by the experimental numerical coefficient of the electron distribution, or rather, we can write

$$k=2r_e\lambda t \tag{3.29}$$

4. Geometrical and Physical Parameters

In the study, it is necessary to distinguish two different intervals. On the one hand, we introduce the *geometric interval* as the distance travelled by the Pioneer-6 signal. It is placed between two points that we define along the path travelled by the radio signal. On the other hand, we define the *physical interval* as the distance travelled by the Pionerer-6 signal up to the next point where at least one interaction between the radio photon and the electrons of the solar corona takes place. Therefore, we can measure it between the values $r_{i\pm\chi}$ and $r_{i\pm1}$. The sign changes depending on whether we are considering the upper part or the lower part of the orbital model as shown in the next equations. By increasing the initial radius with a value of

$$\chi=10^{-3}R_s \tag{4.1}$$

defined as *increment factor*, we will obtain different physical intervals which, added together and imported into the NTL equations, give rise to a series of consecutive values of the interactional redshift. We will later clarify the reason why this exact value has been chosen for the increments. In the procedure of the calculation of the interactional redshift, we can distinguish the following circles, projected on the ecliptic plane, characterized by the following radii:

- r_i: initial geometric radius starting from the position of Earth which initially decreases in the upper part and then increases again in the lower part of the orbital model along the direction of the radio signal;
- $r_{i\pm\chi}$: subsequent initial geometric radius, imposed on the value r_i, having a negative sign in the upper part of the orbital model, since the radii decrease as the signal advances, and having a positive sign in the lower part of the orbital model, due to opposite reasons;
- $r_{i\pm1}$: calculated physical radius in which we find at least one interaction between a photon and an electron having a negative sign in the upper part and a positive sign in the lower part of the orbital model depending on whether the distance, expressed in solar radii, respectively, decreases or increases.

For each above-mentioned radius, there is a corresponding circle. For simplicity of reading, we define the circles with the following indices: i, in the upper part of the orbital model, corresponds to A; $i-\chi$ corresponds to B; $i-1$ corresponds to C; i, in the lower part of the orbital model, corresponds to D; $i+\chi$ corresponds to E and $i+1$ corresponds to F. Each path travelled by the signal, both in the pre-occultation and post-occultation phase, calculated on each measurement day, intersects all three circles into six points in the Cartesian plane resulting from solutions of the quadratic equations shown later. The intersection points are $P_{A,up}(x_{A,up}, y_{A,up})$; $P_{B,up}(x_{B,up}, y_{B,up})$; $P_{C,up}(x_{C,up}, y_{C,up})$; $P_{D,down}(x_{D,down}, y_{D,down})$; $P_{E,down}(x_{E,down}, y_{E,down})$; $P_{F,down}(x_{F,down}, y_{F,down})$.

The y axis is superimposed on the direction between Sun and Earth whereas the x axis is orthogonal to it. We also rotate the ecliptic plane centered in the Sun and place the y axis in a vertical position for improving the visualization. The direction of the x and y axes varies according to the day of measurement, however, as the electron distribution is circular in the plane (as well as spherical in space) the Cartesian axes centered in the Sun will always have the same relative position. As shown in **Figure 11** and **Figure 12**, it will be the path of the radio signal, in the various pre-occultation and post-occultation phases, which crosses the electron corona differently day by day, giving rise to the interactional redshift.

Starting from the points of intersection on the Cartesian plane for each day of measurement, both in the pre-occultation and post-occultation phase, the geometric intervals are equal to:

$$I_{geom,x}^{up} = \sqrt{\left(x_B - x_A\right)^2 + \left(y_A - y_B\right)^2} \tag{4.2}$$

$$I_{geom,x}^{down} = \sqrt{\left(x_E - x_D\right)^2 + \left(y_D - y_E\right)^2} \tag{4.3}$$

We aim to the calculation of the physical intervals, useful for the calculation of the redshift, as follows:

$$I_{phys,x}^{up} = \sqrt{\left(x_B - x_C\right)^2 + \left(y_B - y_C\right)^2} \tag{4.4}$$

$$I_{phys,x}^{down} = \sqrt{\left(x_F - x_E\right)^2 + \left(y_E - y_F\right)^2} \tag{4.5}$$

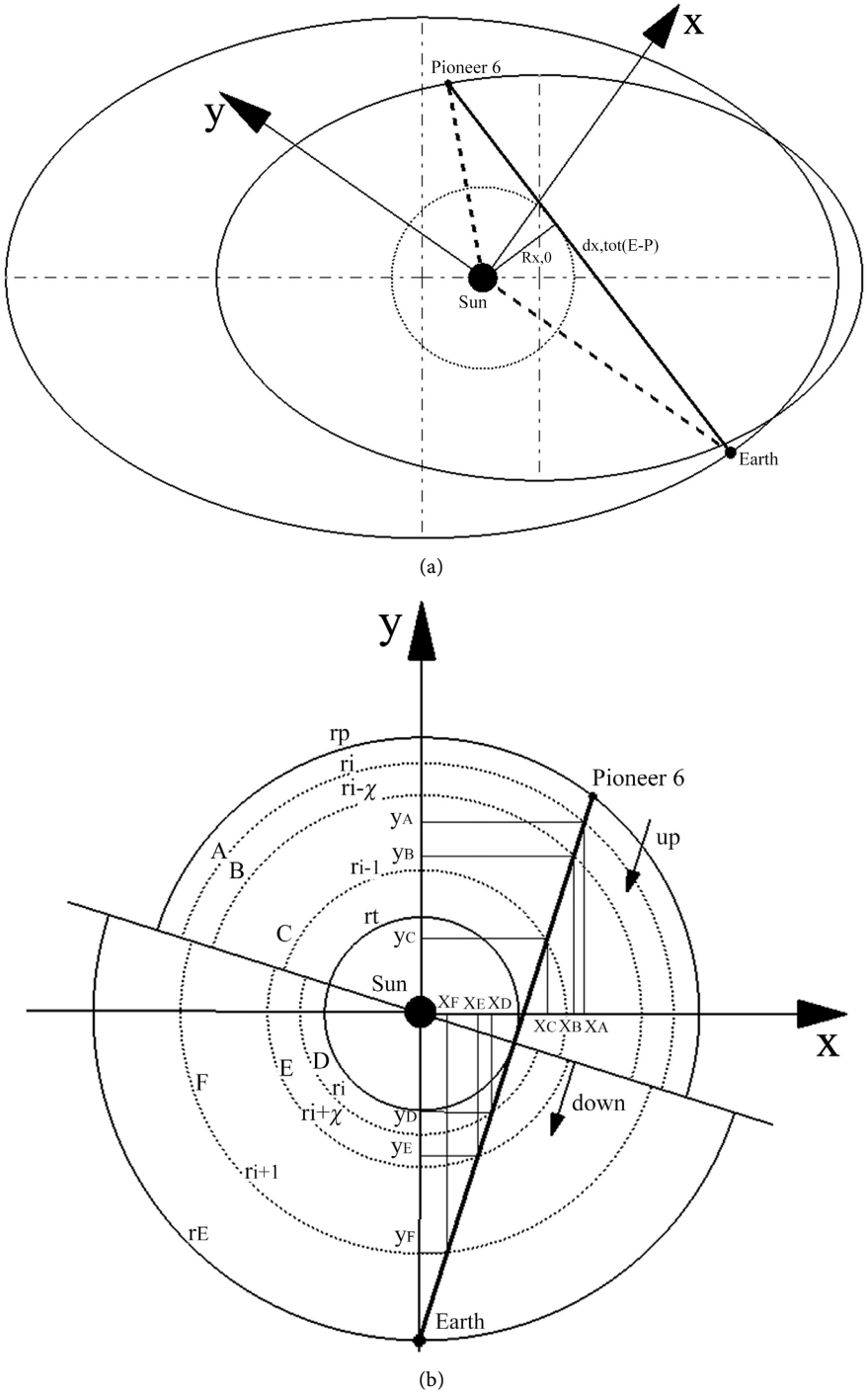

Figure 11. Schematization not on scale of the reference axes and of the geometrical and physical Intervals on a generic measurement day in the pre-occultation phase.

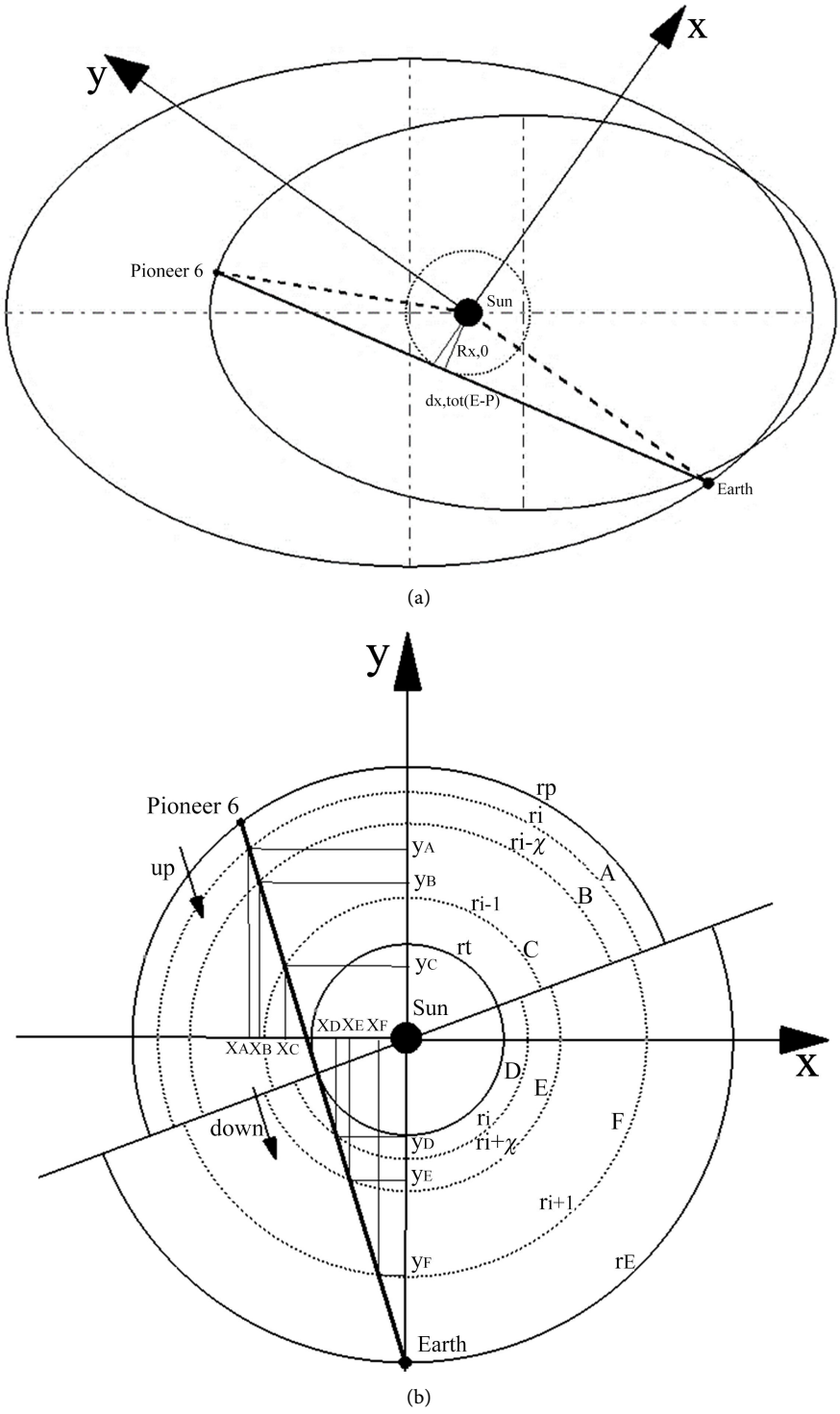

Figure 12. Schematization not on scale of the reference axes and of the geometrical and physical Intervals on a generic measurement day in the post-occultation phase.

For the determination of the physical intervals we calculate the points of intersection between the path of the radio signal, represented by the segment $d_{x,tot}(PE)$, and each reference circle corresponding to a given electron distribution. From these points, we are able to determine the amplitudes travelled by the

radio signal in each circular sector.

In the pre-occultation phase, on a generic day of measurement x, we have the following system characterized by the equation of a circle (intersection of an electron distribution sphere with the ecliptic plane), whose radius increases in the algorithm and meets the segment (path of the radio signal) on the right-hand side of the Sun described by its corresponding line,

$$\begin{cases} x_{x,j}^2 + y_{x,j}^2 = R_x^2 \\ y_{x,j} = +m_x x_{x,j} - q_x \end{cases} \tag{4.6}$$

x and y are the Cartesian coordinates of the radio signal, subscript x indicates the day of measurement considered, $j = i, i-\chi, \cdots, t$ is the index representing the increments and R is the radius calculated from the center of the Sun corresponding to the position of the signal. Moreover, m is the angular coefficient of the line describing the path of the radio signal and q is the intersection of this line with the y axis. From the previous equation, we obtain that:

$$x_{x,j}^2 + \left(m_x x_{x,j} - q_x\right)^2 = R_x^2 \tag{4.7}$$

$$x_{x,j}^2 + m_x^2 x_{x,j}^2 - 2m_x q_x x_{x,j} + q_x^2 = R_x^2 \tag{4.8}$$

$$\left(1+m_x^2\right)x_{x,j}^2 + \left(-2m_x q_x\right)x_{x,j} + \left(q_x^2 - R_x^2\right) = 0 \tag{4.9}$$

It is a quadratic equation that admits the following solutions:

$$x_{x,j,up}^{pre-occ} = \frac{2m_x q_x + \sqrt{\left(-2m_x q_x\right)^2 - 4\left(1+m_x^2\right)\left(q_x^2 - R_x^2\right)}}{2\left(1+m_x^2\right)} \tag{4.10}$$

and

$$x_{x,j,down}^{pre-occ} = \frac{2m_x q_x - \sqrt{\left(-2m_x q_x\right)^2 - 4\left(1+m_x^2\right)\left(q_x^2 - R_x^2\right)}}{2\left(1+m_x^2\right)} \tag{4.11}$$

from which we obtain the corresponding values of y, respectively, as

$$y_{x,j,up}^{pre-occ} = m_x \cdot x_{x,j,up}^{pre-occ} - q_x \tag{4.12}$$

and

$$y_{x,j,down}^{pre-occ} = m_x \cdot x_{x,j,down}^{pre-occ} - q_x \tag{4.13}$$

Similarly, in the post-occultation phase on a generic day of measurement x, this time with $j = i, i+\chi, \cdots, t$, we have other equations and intersection points described by the following system:

$$\begin{cases} x_{x,j}^2 + y_{x,j}^2 = R_x^2 \\ y_{x,j} = -m_x x_{x,j} - q_x \end{cases} \tag{4.14}$$

from which

$$x_{x,j}^2 + \left(-m_x x_{x,j} - q_x\right)^2 = R_x^2 \tag{4.15}$$

$$x_{x,j}^2 + m_x^2 x_{x,j}^2 + 2m_x q_x x_{x,j} + q_x^2 = R_x^2 \tag{4.16}$$

$$\left(1+m_x^2\right)x_{x,j}^2+\left(2m_xq_x\right)x_{x,j}+\left(q_x^2-R_x^2\right)=0 \tag{4.17}$$

It is a quadratic equation that admits the following solutions:

$$x_{x,j,up}^{post-occ}=\frac{-2m_xq_x+\sqrt{\left(2m_xq_x\right)^2-4\left(1+m_x^2\right)\left(q_x^2-R_x^2\right)}}{2\left(1+m_x^2\right)} \tag{4.18}$$

and

$$x_{x,j,down}^{post-occ}=\frac{-2m_xq_x-\sqrt{\left(2m_xq_x\right)^2-4\left(1+m_x^2\right)\left(q_x^2-R_x^2\right)}}{2\left(1+m_x^2\right)} \tag{4.19}$$

from which we obtain the corresponding values of *y*, respectively, as

$$y_{x,j,up}^{post-occ}=-m_x\cdot x_{x,j,up}^{post-occ}-q_x \tag{4.20}$$

and

$$y_{x,j,down}^{post-occ}=-m_x\cdot x_{x,j,down}^{post-occ}-q_x \tag{4.21}$$

5. Interactional Redshift Contribution

The interactional redshift is the increase in wavelength of photons re-emitted by the photo-ionized electrons of the solar corona. The latter act as a medium for the incident photons causing a recoil of the electrons. The incident photons are absorbed and then re-emitted with a small loss of energy. Taking the radio signal as a reference, it has an initial value at the time of emission and then decreases step by step after each interaction. Afterwards, it gets measured by a terrestrial radio receiver. It is possible to identify the interactional redshift from the received signal by removing only the intrinsic gravitational redshift.

5.1. New Tired Light

Referring to the NTL theory of L.E. Ashmore [4] represented in **Figure 13** and customizing the involved factors and equations, according to the radio-anomaly under consideration, we can first of all write the cross-section formula in the absorption and re-emission process equal to

$$\sigma=2r_e\lambda \tag{5.1}$$

where r_e is the classic radius of the electron and λ is the wavelength of the incident photon. The cross-section is not constant but varies along the path travelled by the radio photon as, after each interaction, the wavelength will increase. It represents the probability of the radio signal to encounter an electron along the path from Pioneer-6 to the radio receiver on Earth. This fact implies a mean free path, defined as the length within which we can statistically find at least one interaction between photon and electron, decreasing during the journey of the photon, equal to

$$\Lambda=\frac{1}{\sigma\cdot\overline{n}_e} \tag{5.2}$$

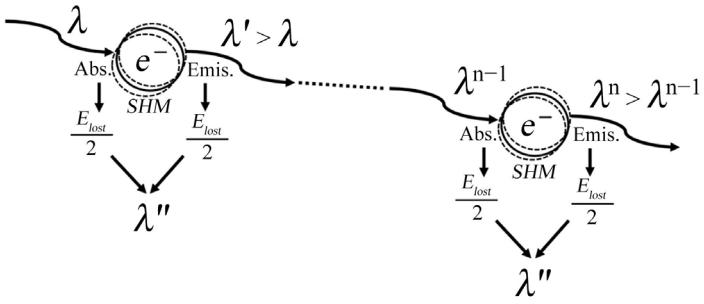

Figure 13. L.E. Ashmore's redshift mechanism proposed in the NTL.

The density of the electrons n_e in this study is an average value within a determined sector covered by the radio signal as described with Equation (3.8) and Equation (3.13). It depends on the zone of the orbital model considered. The single interaction of a photon with an electron determines a constant variation in the wavelength of the photon equal to the Compton length

$$\delta\lambda = \frac{h}{c \cdot m_e} = 2.426 \times 10^{-12}\,\mathrm{m} \tag{5.3}$$

where h is the Planck constant, m_e is the mass of the electron and c is the speed of light. We can point out that the interactional redshift has nothing to do with Compton scattering although the smallest variation in wavelength takes its name. Considering the multiple interactions between the radio photon and the electrons, which the radio photon statistically encounters along its journey to the terrestrial receiver, the total variation of the photon wavelength results as follows:

$$\Delta\lambda = N \cdot \delta\lambda \tag{5.4}$$

$$\Delta\lambda = \frac{I_{phys} \cdot h}{\Lambda \cdot c \cdot m_e} \tag{5.5}$$

where N is the number of total interactions in the physical interval I_{phys} described in the previous paragraph and Λ is the mean free path. The redshift at the end of the interactions will therefore be calculated as the variation in the wavelength of the signal with respect to its initial length:

$$z = \frac{\Delta\lambda}{\lambda} \tag{5.6}$$

$$z = \frac{I_{phys} h}{\Lambda c \cdot m_e \lambda} \tag{5.7}$$

$$z = \frac{2 r_e \lambda \overline{n}_e I_{phys} h}{c \cdot m_e \lambda} \tag{5.8}$$

$$z = \frac{2 r_e \overline{n}_e I_{phys} h}{c \cdot m_e} \tag{5.9}$$

The Hubble constant represents, for the first time in history, a loss of energy as a function of fundamental parameters as shown in the following formula

$$H = 2\overline{n}_e \frac{h \cdot r_e}{m_e} \tag{5.10}$$

Depending on the density of the electrons through which the photons travel, the Hubble constant will assume different values.

Furthermore, according to the interactional process in NTL, a secondary photon is also expected as a result of the transfer of energy to the surrounding environment following the recoil of the electron, once it is at rest. The value obtained, considering the radio signal emitted by the Pioneer-6 space probe, is too huge to argue about a real secondary photon. It is likely valid for photons having shorter wavelengths in other fields of the light spectrum. The formula that expresses the secondary photon, which we will not deal in detail and which is beyond the scope of this study, is the following

$$\lambda'' = \frac{2m_e c\lambda^2}{h} \tag{5.11}$$

Returning to the basics of the theory, the first fundamental condition for an electron in the plasma of the solar corona in order to re-emit a photon is the following:

$$\nu_{P6} > \nu_{res,e^-} \tag{5.12}$$

$$\frac{c}{\lambda_{P6}} > \frac{1}{2\pi}\sqrt{\frac{\overline{n}_e e^2}{m_e \varepsilon_0}} \tag{5.13}$$

The frequency of the incident radio photon is greater than the resonance frequency of the electron in the plasma in the area of the solar corona under examination. Regarding the coefficients: e is the electric charge of the electron and ε_0 is the permittivity in free space. All the values of the constants are contained in **Appendix A**. The previous condition is always verified in all areas of interest of the solar corona as shown later in **Table 6**. Moving forward towards the recent developments of the NTL theory [5] by the English physicist, a further essential condition for the interactions between photons and electrons, based on the concepts in the field of solid-state physics of E.P. Wigner [16] [17], has to be verified in order to observe an NTL process taking place:

$$\mathrm{PE}_e \geq \mathrm{KE}_e \tag{5.14}$$

The potential energy of the electron has to be greater than its kinetic energy so that the electrons of the solar corona can form the Wigner Crystal as schematized in **Figure 14**. Although the theory is particularly suitable for low temperatures, especially for L.E. Ashmore's field of study in the IGM with electron density of 0.5 el/m^3 and temperature of $T = 2.73$ K, this cannot exclude the fact that we can theorize a similar mechanism of TL at much higher density and temperatures in the solar corona. The physical characteristics of the crystal allow the photons to pass through it without deviating from the original direction. They travel accordingly along a straight trajectory and without image blurring: fundamental characteristics distinguishing NTL from other scattering processes.

By explicitly developing the relative expressions of potential and kinetic energy, we can calculate the radius of the sphere surrounding the electron that verifies the previous condition where k_B is the Boltzmann constant and T_e is the

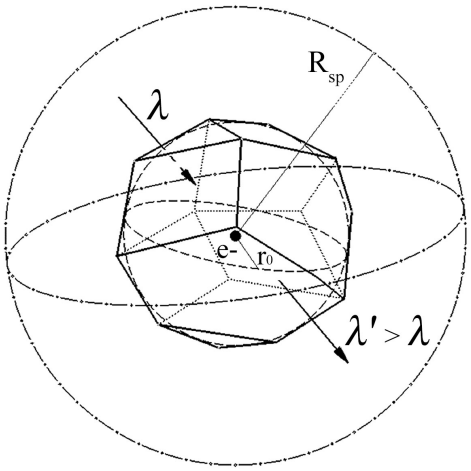

Figure 14. Schematization of a Wigner crystal centered in an electron.

Table 6. Generic instance of NTL parameters in function of the physical characteristics of radio signal and solar corona. *y*: verified, *n*: not verified.

$\nu_{P6} > \nu_{res,e^-}$ $PE_u > KE$ $R_{sp} > r_0$		n_e [el/m^3]			
		1E+11	1E+10	1E+09	1E+08
		T_e [K]			
		1.5E+06	1E+06	8E+05	5E+05
ν_{P6}	[Hz]	2.292E+09	2.292E+09	2.292E+09	2.292E+09
ν_{res,e^-}	[Hz]	2.839E+06	8.979E+05	2.839E+05	8.979E+04
$\nu_{P6} > \nu_{res,e^-}$	[Hz]	*y*	*y*	*y*	*y*
PE/R_{sp}^2	[J/m^2]	1.449E-16	1.449E-17	1.449E-18	1.449E-19
KE	[J]	3.105E-17	2.07E-17	1.656E-17	1.04E-17
R_{sp}	[m]	0.463	1.195	3.380	8.450
PEu	[J]	6.709E-17	1.732E-17	4.899E-18	1.225E-18
r_0	[m]	0.000134	0.000288	0.000620	0.001337
$PE_u > KE$	[J]	*y*	*n*	*n*	*n*
$R_{sp} > r_0$	[m]	*y*	*y*	*y*	*y*

$$\frac{\overline{n}_e e^2}{2\varepsilon_0} R_{sp}^2 \geq \frac{3}{2} k_B T_e \tag{5.15}$$

$$R_{sp} \geq \frac{1}{e}\sqrt{\frac{3k_B T_e \varepsilon_0}{\overline{n}_e}} \tag{5.16}$$

temperature of the electrons in the considered area of the solar corona [18] at average density n_e. We can extract the graph of the temperature trend as the distance from the Sun changes as shown in Figure 15.

The radius R of the sphere has to be, in turn, greater than the minimum radius of the Wigner-Seitz sphere around which the Body Centered Cubic (BCC) lattice is established.

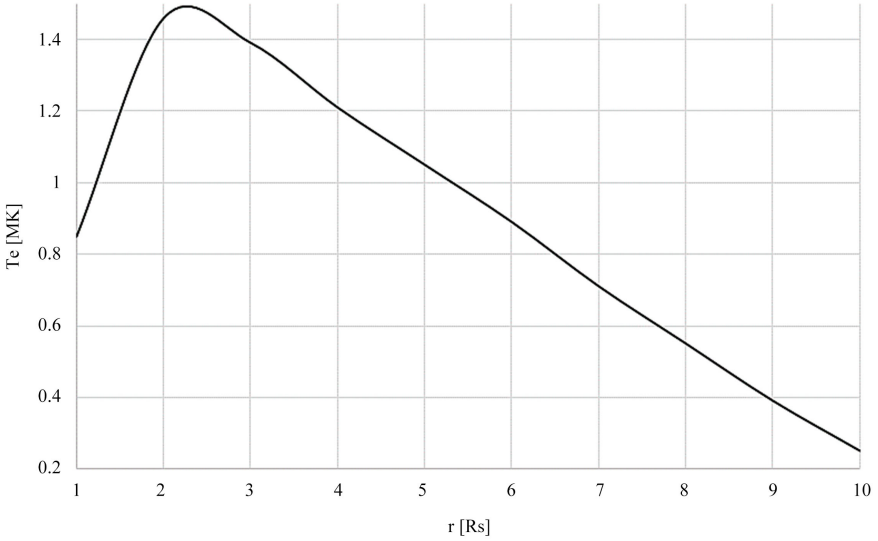

Figure 15. Transcription from R.L. Alexander *et al.* of the approximated electron temperature trend for different solar radii.

$$R_{sp} > r_0 \tag{5.17}$$

$$\frac{1}{e}\sqrt{\frac{3k_B T_e \varepsilon_0}{\bar{n}_e}} > \sqrt[3]{\frac{3}{4\pi \bar{n}_e}} \tag{5.18}$$

The condition is largely verified for all areas of the solar corona taken into consideration as shown in **Table 6**. In this way, the radio photon can pass from one electron to the next one, both embedded into a crystal. Thanks to sufficient space, this allows the recoil of the electron described by a Simple Harmonic Motion (SMH). Moreover, we can calculate the corresponding velocity of the electron through the following two expressions of the kinetic energy.

$$\mathrm{KE}_{e,T} = \mathrm{KE}_{e,v} \tag{5.19}$$

$$\frac{3}{2}k_B T_e = \frac{1}{2}m_e v_e^2 \tag{5.20}$$

$$v_e = \sqrt{\frac{3k_B T_e}{m_e}} \tag{5.21}$$

We can trace the radius of the sphere in correspondence to this direction of motion, and according to this study, we consequently place a further restrictive condition that we define as Wigner-Crystal Precondition:

$$\mathrm{PE}_{e,u} \geq \mathrm{KE}_{e,v} \tag{5.22}$$

or namely the unitary potential energy (per unit radius of the sphere) of the electron has to dominate its kinetic energy along the same direction. In the previous equation, by explaining explicitly the involved terms, we obtain:

$$\frac{\frac{\bar{n}_e e^2}{2\varepsilon_0} R_{sp}^2}{R_{sp}} \geq \frac{1}{2}m_e v_e^2 \tag{5.23}$$

$$\frac{\overline{n}_e e^2}{2\varepsilon_0} R_{sp} \geq \frac{1}{2} m_e v_e^2 \tag{5.24}$$

It is an admissible condition due to the fact that we have reduced the spatial interactions between radio photon and electrons to a one-dimensional problem along a specific trajectory in the solar corona. If this restrictive condition is also verified, then the crystallization of the electron, according to Wigner in the NTL process, can take place. In the summary of Table 6, we can list all the parameters introduced so far to verify the conditions for NTL.

The calculations demonstrate that NTL is only valid where there is a simultaneous specific combination of the densities and temperatures shown in the first column on the left. This allows us to exclude the remaining columns corresponding to lower redshift contributions from the calculations. The verification of the Wigner-Crystal precondition for all admissible combinations between n_e and T_e is shown in detail in Table 7.

Table 7. Verification of Wigner-Crystal precondition for all possible admissible combinations between ne and Te. y: verified, n: not verified.

$PE_u > KE$		T_e [K]								
		9.00E+06	8.00E+06	7.00E+06	6.00E+06	5.00E+06	4.00E+06	3.00E+06	2.00E+06	1.00E+06
	1E+12	*y*	*y*	*y*	*y*	*y*	*y*	*y*	*y*	*y*
	1E+11	*n*	*n*	*y*	*y*	*y*	*y*	*y*	*y*	*y*
	1E+10	*n*	*n*	*n*	*n*	*n*	*n*	*n*	*n*	*n*
	1E+09	*n*	*n*	*n*	*n*	*n*	*n*	*n*	*n*	*n*
	1E+08	*n*	*n*	*n*	*n*	*n*	*n*	*n*	*n*	*n*
	1E+07	*n*	*n*	*n*	*n*	*n*	*n*	*n*	*n*	*n*
	1E+06	*n*	*n*	*n*	*n*	*n*	*n*	*n*	*n*	*n*
		9.00E+05	8.00E+05	7.00E+05	6.00E+05	5.00E+05	4.00E+05	3.00E+05	2.00E+05	1.00E+05
	1E+12	*y*	*y*	*y*	*y*	*y*	*y*	*y*	*y*	*y*
	1E+11	*y*	*y*	*y*	*y*	*y*	*y*	*y*	*y*	*y*
	1E+10	*n*	*n*	*y*	*y*	*y*	*y*	*y*	*y*	*y*
n_e [el/m^3]	1E+09	*n*	*n*	*n*	*n*	*n*	*n*	*n*	*n*	*n*
	1E+08	*n*	*n*	*n*	*n*	*n*	*n*	*n*	*n*	*n*
	1E+07	*n*	*n*	*n*	*n*	*n*	*n*	*n*	*n*	*n*
	1E+06	*n*	*n*	*n*	*n*	*n*	*n*	*n*	*n*	*n*
		9.00E+04	8.00E+04	7.00E+04	6.00E+04	5.00E+04	4.00E+04	3.00E+04	2.00E+04	1.00E+04
	1E+12	*y*	*y*	*y*	*y*	*y*	*y*	*y*	*y*	*y*
	1E+11	*y*	*y*	*y*	*y*	*y*	*y*	*y*	*y*	*y*
	1E+10	*y*	*y*	*y*	*y*	*y*	*y*	*y*	*y*	*y*
	1E+09	*n*	*n*	*y*	*y*	*y*	*y*	*y*	*y*	*y*
	1E+08	*n*	*n*	*n*	*n*	*n*	*n*	*n*	*n*	*n*
	1E+07	*n*	*n*	*n*	*n*	*n*	*n*	*n*	*n*	*n*
	1E+06	*n*	*n*	*n*	*n*	*n*	*n*	*n*	*n*	*n*

In the opposite case, in which the kinetic energy dominates the potential energy of the crystal, we can write that

$$\mathrm{PE}_{e,u} < \mathrm{KE}_{e,v} \tag{5.25}$$

We can therefore define the difference between the two energies as the kinetic energy in excess described in the following formula:

$$\Delta\mathrm{KE}_{e,exc} = \mathrm{KE}_{e,v} - \mathrm{PE}_{e,u} \tag{5.26}$$

$$\Delta\mathrm{KE}_{e,exc} = \frac{1}{2} m_e v_e^2 - \frac{\overline{n}_e e^2}{2\varepsilon_0} R_{sp} \tag{5.27}$$

Once calculated this value, we can determine the velocity in excess, in m/sec, associated to it from the expression

$$\Delta\mathrm{KE}_{e,exc} = \frac{1}{2} m_e v_{e,exc}^2 \tag{5.28}$$

$$v_{e,exc} = \sqrt{\frac{2 \cdot \Delta\mathrm{KE}_{e,exc}}{m_e}} \tag{5.29}$$

$$v_{e,exc} \cong 10^{-25} \cong 0 \tag{5.30}$$

Thus, in the temperature range where the Wigner-Crystal Precondition is not satisfied, this excludes the transfer of energy from the electrons to the radio photons which would have probably resulted in a blueshift of the radio signal. In these zones, the energy of the incident photon is equal to the energy of the re-emitted photon. Therefore, the radio photons undergo a Thomson scattering process with the electrons in the solar corona before approaching NTL areas. Depending on the combination of temperature and electron density, where the Wigner-Crystal Precondition is satisfied, Wigner crystals get formed. Through them, photons can travel on a straight line. A single radio photon is absorbed and re-emitted by electrons surrounded by crystals. In the process, a loss of energy takes place and gives rise to an interactional redshift after multiple interactions between the radio photon and electrons. It is what the radio receiver detects on Earth together with the gravitational redshift.

5.2. Computational Method Applied

The calculation of redshift is not linear but turns out to be the sum of different contributions. The redshift trend is therefore a function of many parameters such as the length of the signal path, function of the elliptical orbital dynamics between Earth and Pioneer-6, the exponential-variable density of electrons in the solar corona and the wavelength of the signal. The latter increases interaction by interaction. Generally, we detect thousands of redshift values of the order of 1E-11 starting from the position of the Pioneer-6 space probe, where there is a low electron density. Moving towards the Sun, we encounter dozens of redshift orders equal to 1E-10 and only one value of the order equal to 1E-09 precisely as the electron density is greater in the vicinity of the Sun. Furthermore, we can ex-

clude all redshift contributions, generally those of the order of 1E-11 and some of the order 1E-10 that do not satisfy the Wigner-Crystal Precondition of Equation (5.22) for the calculation of the total interactional redshift. It means that the calculation of the total redshift is not reduced to a simple algebraic sum but has to be weighed carefully according to a very specific criterion. Firstly, we exclude the values that do not satisfy the Wigner-Crystal Precondition and then we apply a criterion lent to us by another scientific field. The principle is similar to the one used in mechanical engineering in the Finite Element Method (FEM) for which, in order to calculate more specific and punctual stress-deformation values of the material, it is necessary to increase the mesh. In fact, it happens that previous to the first round of calculation high stress-deformations are expected in some points of the material subject to very high loads or where the geometry, in turn, induces very high stresses. These values are, however, too small at the beginning. The operator acts by thickening the mesh in the critical areas of the component, thus achieving the expected result. It is possible to make very precise parallelism with this study of the interactions between the radio signal and the photo-ionized electrons in the solar corona for the calculation of the redshift. As the electron density is higher in the vicinity of the Sun and as the corresponding redshift values are consequently higher, it means that we have to focus our calculation window in this area, reducing it to a few calculation cells and then extract the key redshift values that provide a greater weight to the total redshift. On the contrary, we extend the calculation window away from the Sun, including many calculation cells, where the redshift values are two orders of magnitude smaller and therefore provide a minor impact to the total redshift. We define this method as *Mesh Approach* which is possible to apply as we implement the redshift calculation according to χ increments. Before proceeding with the calculation of the redshift, however, it is necessary to make some observations on the increment factor set in Equation (4.1) and on the reason why this value has been chosen. This value allows us to make increases in the intervals, aiming at redshift calculations, with a lower expenditure of energy for the operator and the calculator. Going further towards increment values equal to 1E-04 or 1E-05 solar radii, the computing time takes too long. A workstation dedicated only to this type of calculation would serve this purpose. In any case, the redshift values obtained with increments of the order of 1E-03 solar radii are sufficient enough to allow its use in this study. In fact, we can state that

$$\lim_{\chi \to 0} z = z_{\lim} \quad \forall \lambda \tag{5.31}$$

For lower values of the increase, the redshift tends to a limit value for every specific reference wavelength. It is valid only in one direction of calculation and not, for instance, along two calculation directions (e.g., upper and lower part of the orbital model simultaneously).

We can start with the calibration of the redshift calculation method on each measurement day starting from 1968 November 6, first day of measurements, and extracting the redshift values at close distances from the Sun. In these areas,

the redshift provides the dominant contributions for the total calculation. In practice, we define two columns next to the redshift in which we number respectively, on the left, the row index *ro* of the calculation in the spreadsheet and, on the right, the cell index *ce*. The latter starts from 0 and not from 1 as we will sum up the redshift exponentially starting from the first cell (exp(0) = 1). Furthermore, this last column, in the upper part of the orbital model, has an inverted number order with respect to the computation row indices.

Observing Table 8, for the upper part of the orbital model on 1968 November 6, considering the redshift according to the cell indices, we can calculate that:

$$\sum_{ce=0}^{ce_{\lim}} z_{e^{ce}} = z_{e^0} + z_{e^1} + \cdots + z_{e^{12}} \tag{5.32}$$

$$\sum_{0}^{12} z_{e^{ce}} = z_1 + z_{2.72} + \cdots + z_{162754.79} \tag{5.33}$$

From Table 9, as the total cells ce_{tot} extracted by the Wigner-Crystal Precondition is 1838 and by taking into account the real ce_{lim} being the max integer exponential is 1097 from cell number 7, the formula becomes:

$$\sum_{0}^{7} z_{e^{ce}} \approx z_1 + z_3 + \cdots + z_{1097} \tag{5.34}$$

$$\sum_{0}^{7} z_{e^{ce}} \approx 3.36 \times 10^{-9} \tag{5.35}$$

Also, by identifying the redshift through the row indices, we can write that:

$$\sum_{ro_{\lim}}^{ro_{\lim}-(n-1)} z_{ro} = z_{174798} + z_{174797} + z_{174796} \tag{5.36}$$

$$\sum_{174798}^{174796} z_{ro} = 3.29 \times 10^{-9} \tag{5.37}$$

Table 8. Interactional redshift extract from 1968 November 6, upper part (left side) and lower part (right side) of the orbital model.

1	1.857887004E-11	174,797	ro [row]	z [-]	ce [cell]
2	1.857887034E-11	174,796	1	**9.88941786E-10**	0
3	1.857887063E-11	174,795	2	**7.88947519E-10**	1
4	1.857887092E-11	174,794	3	**6.75736588E-10**	2
5	1.857887122E-11	174,793	4	6.00509611E-10	3
…..	…...	…….	5	5.45881001E-10	4
174,791	4.703378535E-10	7	6	5.03892891E-10	5
174,792	5.039129882E-10	6	7	4.70318793E-10	6
174,793	5.459022989E-10	5	8	4.42678470E-10	7
174,794	6.005323020E-10	4	…..	…...	…….
174,795	6.757608462E-10	3	202,421	1.88379256E-11	202,420
174,796	**7.889732743E-10**	2	202,422	1.88379256E-11	202,421
174,797	**9.889671942E-10**	1	202,423	1.88379256E-11	202,422
174,798	**1.515016758E-09**	0	202,424	1.88379256E-11	202,423
ro [row]	z [-]	ce [cell]	202,425	1.88379256E-11	202,424

Table 9. Definition of a criterion for the row count for pre-occultation and post-occultation phase.

$n_{e,\max}$	Linear factor L	$\psi = L^{c-1}$	ce_{up} and ce_{down} (pre-occultation)	ce_{up} and ce_{down} (post-occultation)
[el/m^3]	[-]	[-]	[cells]	[cells]
$5\times10^{+9} \le n_{e,\max} \le 1\times10^{+10}$	1 ÷ 2	1 ÷ 3	$3\cdot\psi$	$5\cdot\psi$
$1\times10^{+10} \le n_{e,\max} \le 2\times10^{+10}$	2 ÷ 4	3 ÷ 8		
$2\times10^{+10} \le n_{e,\max} \le 4\times10^{+10}$	4 ÷ 8	8 ÷ 25		
$4\times10^{+10} \le n_{e,\max} \le 8\times10^{+10}$	8 ÷ 16	25 ÷ 72		
$8\times10^{+10} \le n_{e,\max} \le 8\times10^{+11}$	16 ÷ 32	72 ÷ 208		

$$z_{up,6Nov}^{ntl} = 3.29\times10^{-9} \tag{5.38}$$

where

$$n = 3 \tag{5.39}$$

We can point out that row 174,798 corresponds to the value of r_t expressed in solar radii for which there is the transition from the upper to the lower part of the orbital model and where the calculation of the redshift stops in the upper part of the orbital model in the spreadsheet. In this way, there is a clear analogy between the redshift calculation and the two methods, described by

$$\sum_{ce=0}^{ce_{\lim}} z_{e^{ce}} \approx \sum_{ro_{\lim}}^{ro_{\lim}-3} z_{ro} \tag{5.40}$$

This implies that the number of cells to be taken into account in the calculation of the redshift is

$$ce_{up}^{pre-occ} = 3 \text{ rows} \tag{5.41}$$

For the lower part of the orbital model, considering the redshift, according to the cell indices, we calculate that:

$$\sum_{ce=0}^{ce_{\lim}} z_{e^{ce}} = z_{e^0} + z_{e^1} + \cdots + z_{e^{12}} \tag{5.42}$$

$$\sum_{0}^{12} z_{e^{ce}} = z_1 + z_{2.72} + \cdots + z_{162754.79} \tag{5.43}$$

For the same reason explained after Equation (5.33), the formula becomes:

$$\sum_{0}^{7} z_{e^{ce}} \approx z_1 + z_3 + \cdots + z_{1097} \tag{5.44}$$

$$\sum_{0}^{7} z_{e^{ce}} \approx 2.49\times10^{-9} \tag{5.45}$$

Also, by identifying the redshift through the row indices, we observe that:

$$\sum_{ro=1}^{ro+(n-1)} z_{ro} = z_1 + z_2 + z_3 \tag{5.46}$$

$$\sum_{1}^{3} z_{ro} = 2.45\times10^{-9} \tag{5.47}$$

$$z_{down,6Nov}^{ntl} = 2.45\times10^{-9} \tag{5.48}$$

where

$$n = 3 \tag{5.49}$$

Thus, there is a clear analogy between the redshift calculation and the two methods, described by

$$\sum_{ce=0}^{ce_{\lim}} z_{e^{ce}} \approx \sum_{ro=1}^{ro+(n-1)} z_{ro} \tag{5.50}$$

This implies that the number of cells to be taken into account in the calculation of the redshift is

$$ce_{down}^{pre-occ} = 3 \text{ rows} \tag{5.51}$$

Therefore, from calibration, we can use the following minimum number of rows on each day of calculation starting from 1968 November 6:

$$ce_{\min,x}^{pre-occ} = ce_{up}^{pre-occ} + ce_{down}^{pre-occ} \tag{5.52}$$

$$ce_{\min,x}^{pre-occ} = 6 \text{ rows} \tag{5.53}$$

where $x = 1, 2, \cdots, 12$ according to the indexed days in the pre-occultation phase. In practice, the calculation of the total redshift is reduced to the sum of well-established lines which easily improve the calculations. However, the value of the determined lines has to be proportional to the density of the electrons in question. In fact, as can be observed in Table 10, it varies on each measurement day. We can define a criterion to assign the right number of rows to add up in order to get the total redshift. Getting closer to the Sun, the following relations are valid

$$z \propto n_e \propto r^{\varepsilon-1} \propto ce^{\varepsilon-1} \tag{5.54}$$

where with *ce*, we indicate the cell index. Then we will introduce the *interpolation factor* ψ which takes into account the variation to the power $\varepsilon - 1$. This factor establishes how much we need to thicken the calculation according to the Mesh Approach. The values chosen in the new calculation window do not have to contradict the Wigner-Crystal Precondition of Equation (5.22).

In the case of the post-occultation phase, the distances between Earth and Pioneer-6 are 1% smaller than the pre-occultation phase distances as shown in Figure 5. Therefore, the redshift calculation is more compressed into a smaller geometric interval, compared to that of 1968 November 6 used for calibration, whereby the redshift density per unit of length is greater. As a matter of fact, in the post-occultation phase the signal is already emitted in a solar atmosphere with a higher density of electrons. The latter causes a sudden increase in the wavelength and consequently in the redshift. In the pre-occultation phase, however, the redshift is spread over larger distances which will make the curve smoother. From the Wigner-Crystal Precondition, the number of redshift values that satisfy the condition is higher. Due to this fact, it is necessary to increase proportionally the impact in terms of redshift by setting up a proper number of total rows equal to

$$ce_{up}^{post-occ} = ce_{down}^{post-occ} = 5 \text{ rows} \tag{5.55}$$

from which, starting from 1968 November 29, we obtain the following minimum number of lines on each measurement day:

Table 10. Admissible rows and cells for the interactional redshift according to, respectively, the Wigner-Crystal Precondition and the Mesh Approach.

Parameters															
Pre-occultation phase												Post-occultation phase			
rotot, do	rotot, up	Te, min, down	Te, min, up	rmax, do	rmax, up	ne, min, down	ne, min, up	Te, max	rmin	ne, max	x	date	rotot, do	rotot, up	Te, min, down	Te, min, up	rmax, do	rmax, up	ne, min, down	ne, min, up	Te, max	rmin	ne, max	x	date
[rows]	[rows]	[K]	[K]	[Rs]	[Rs]	[el/m^3]	[el/m^3]	[K]	[Rs]	[el/m^3]	[indexed day]	[calender day]	[rows]	[rows]	[K]	[K]	[Rs]	[Rs]	[el/m^3]	[el/m^3]	[K]	[Rs]	[el/m^3]	[indexed day]	[calender day]
202,425	174,797	n.a.	n.a.	213	184	2.3E+06	3.3E+06	2.5E+05	9.96	5.0E+09	1	Nov 06, 1968	207,188	173,799	n.a.	n.a.	212	177	2.3E+06	3.6E+06	1.2E+06	−4.20	5.0E+10	13	Nov 29, 1968
203,222	175,165	n.a.	n.a.	213	184	2.3E+06	3.3E+06	4.0E+05	9.30	6.5E+09	2	Nov 07, 1968	206,387	172,853	n.a.	n.a.	212	177	2.3E+06	3.6E+06	1.0E+06	−4.86	3.5E+10	14	Nov 30, 1968
203,461	175,257	n.a.	n.a.	213	183	2.3E+06	3.3E+06	5.0E+05	8.78	7.5E+09	3	Nov 08, 1968	205,755	172,077	n.a.	n.a.	212	177	2.3E+06	3.6E+06	9.5E+05	−5.49	2.5E+10	15	Dec 01, 1968
204,042	175,537	n.a.	n.a.	213	183	2.3E+06	3.4E+06	6.0E+05	8.21	9.0E+09	4	Nov 09, 1968	205,186	171,221	n.a.	n.a.	212	176	2.3E+06	3.7E+06	9.0E+05	−6.06	2.0E+10	16	Dec 02, 1968
204,729	175,806	n.a.	n.a.	213	182	2.3E+06	3.4E+06	6.5E+05	7.51	1.1E+10	5	Nov 10, 1968	204,525	171,416	n.a.	n.a.	212	176	2.3E+06	3.7E+06	8.0E+05	−6.72	1.5E+10	17	Dec 03, 1968
205,940	176,018	n.a.	n.a.	213	182	2.3E+06	3.4E+06	7.0E+05	7.01	1.3E+10	6	Nov 11, 1968	203,814	169,703	n.a.	n.a.	211	176	2.3E+06	3.7E+06	7.0E+05	−7.29	1.2E+10	18	Dec 04, 1968
205,711	176,355	n.a.	n.a.	213	182	2.3E+06	3.4E+06	9.0E+05	6.39	1.7E+10	7	Nov 12, 1968	203,123	168,725	n.a.	n.a.	211	176	2.3E+06	3.7E+06	6.0E+05	−7.98	9.5E+09	19	Dec 05, 1968
206,340	176,553	n.a.	n.a.	212	181	2.3E+06	3.4E+06	9.5E+05	5.76	2.2E+10	8	Nov 13, 1968	202,455	167,913	n.a.	n.a.	211	176	2.3E+06	3.7E+06	5.0E+05	−8.65	7.9E+09	20	Dec 06, 1968
206,797	176,865	n.a.	n.a.	212	181	2.3E+06	3.4E+06	1.0E+06	5.16	3.0E+10	9	Nov 14, 1968	201,814	167,128	n.a.	n.a.	211	175	2.3E+06	3.7E+06	4.0E+05	−9.29	6.6E+09	21	Dec 07, 1968
207,419	177,199	n.a.	n.a.	212	181	2.3E+06	3.4E+06	1.1E+06	4.54	4.1E+10	10	Nov 15, 1968													
207,804	177,439	n.a.	n.a.	212	180	2.3E+06	3.5E+06	1.2E+06	4.01	5.6E+10	11	Nov 16, 1968													
208,916	177,978	n.a.	n.a.	212	180	2.3E+06	3.5E+06	1.4E+06	3.04	1.1E+11	12	Nov 17, 1968													

Celim Mesh Approach [cells]	cetot Wi.-Cr. Precond [cells]	ne, lim Wi.-Cr. Precond [el/m^3]
1097	1838	3.6E+09
403	474	5.8E+09
148	250	7.1E+09
148	198	8.5E+09
1097	713	9.0E+09
1097	879	1.0E+10
1097	1211	1.1E+10
1097	1152	1.4E+10
1097	1566	1.5E+10
2981	2019	1.6E+10
2981	2249	1.8E+10
2981	3869	1.4E+10
2981	2060	1.8E+10
1097	1867	1.5E+10
1097	1420	1.4E+10
1097	1056	1.3E+10
1097	1623	1.2E+10
403	600	1.0E+10
403	393	8.6E+09
403	331	7.2E+09
403	488	5.8E+09

$$ce_{\min,x}^{post-occ} = ce_{up}^{post-occ} + ce_{down}^{post-occ} \tag{5.56}$$

$$ce_{\min,x}^{post-occ} = 10 \text{ rows} \tag{5.57}$$

where $x = 13,14,\cdots,21$ according to the indexed days in the post-occultation phase. For instance, if we consider a generic observation day in the upper part of the orbital model (we would make similar remarks for the lower part of the orbital model), observing the consecutive redshift trend in the spreadsheet, as shown in Figure 16, we can state how the curve has a peak in correspondence to a few lines of calculation compared to the entire initial calculation window. This implies that the redshift is concentrated close to the Sun where the distance between the radio signal and the Sun is smaller. Furthermore, we can exclude the whole series of minor redshift contributions as they do not satisfy the Wigner-Crystal Precondition. Due to the exclusion of most of the contributions to the redshift, we should start again with the nominal value of the radio wavelength in the calculations. Nevertheless, we leave the current value obtained from consecutive interactions which differs by a small value compared to the nominal one. In this way, we do not re-launch the calculations. The redshift values calculated in this way remain reliable. This approach is valid for each measurement day with clearly different redshift values depending on the distance and therefore on the average distribution of electrons crossed.

For each measurement day, it is possible to calculate firstly the electron density limit (going deeply into in-between values of Table 7) from which we can detect the number of total rows to take into account for the redshift calculation, as shown in Table 10. It contains the complete calculation in the spreadsheet including the admissible rows and cells for the interactional redshift according to, respectively, the Wigner-Crystal Precondition and the Mesh Approach. As the redshift is calculated on a consecutive manner, the effective number of rows which will compose the interactional redshift is much smaller according to the Mesh Approach.

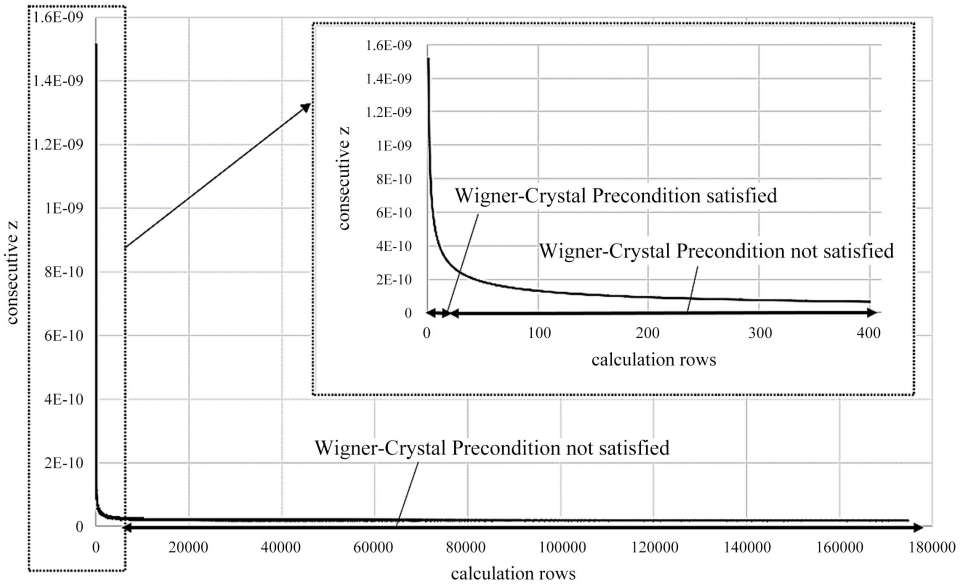

Figure 16. Instance of a consecutive redshift trend, with the Precondition exclusions, as result of the calculations on a generic measurement day.

6. Gravitational Redshift Contribution

The contribution of the gravitational redshift, in addition to the interactional redshift, is the only one that we can also include in the calculations as the Doppler contributions of the orbital and rotational velocities can be neglected in the radio-receiver. We can use a Newtonian approach as, for small distances like those of the Sun-Earth-Pioneer-6 system, the gravitational field is the same by using an Einsteinian approach from General Relativity. For this reason, from the conservation of the total energy, we can obtain the value of the wavelength leaving a gravitational field as follows:

$$E_{tot} = \mathrm{KE} + \mathrm{PE} \tag{6.1}$$

$$E_{tot} = h\nu - \frac{Gm_{ph}M_S}{d_x} \tag{6.2}$$

$$E_{tot} = h\nu - \frac{GM_S}{d_x}\frac{h\nu}{c^2} \tag{6.3}$$

$$E_{tot} = h\nu\left(1 - \frac{GM_S}{d_x c^2}\right) \tag{6.4}$$

$$E_{tot} = h\nu' \tag{6.5}$$

In terms of gravitational redshift, the expression becomes:

$$z_{gr} = \frac{\lambda' - \lambda}{\lambda} \tag{6.6}$$

$$z_{gr} = \frac{\dfrac{\lambda}{\left(1 - \dfrac{GM_S}{d_x c^2}\right)} - \lambda}{\lambda} \tag{6.7}$$

If referred to a generic measurement day x, the formula is expressed as

$$z_{gr,x}^{Sun} = \frac{1}{\left(1-\frac{GM_S}{d_x c^2}\right)} - 1 > 0 \tag{6.8}$$

A photon of light loses energy by escaping the gravitational field of the Sun, therefore, its wavelength becomes longer (redshift), whereas it gains energy by approaching the gravitational field of the Earth, the reason why its wavelength becomes shorter (blueshift). We express, accordingly, the gravitational redshift for the Earth by the following expression

$$z_{gr,x}^{Earth} = \frac{1}{\left(1-\frac{GM_E}{R_E c^2}\right)} - 1 < 0 \tag{6.9}$$

7. Total Redshift Calculation

Based on the maximum electron distribution found at the closest distance from the Sun, we can determine the exact value of the linear interpolation factor ψ from Table 9. Considering all the steps previously analyzed, we determine total redshift values which are possible to compare with existing values from other studies, including the observational data that represents our main comparison target

$$z_{tot,x}^{E/P6} = z_{up,x}^{ntl} + z_{down,x}^{ntl} + z_{gr,x}^{Sun} + z_{gr,x}^{Earth} \tag{7.1}$$

As, between pre-occultation and post-occultation phase, the total number of measurements days vary from $x = 1, 2, \cdots, 21$, we can calculate twenty-one redshift contributions. All calculations relating to redshift in the pre-occultation and post-occultation phase are shown in Table 11 whereas the complete list of calculations in the spreadsheet is meticulously reported in **Appendix B**.

Table 11. Partial and total redshift calculations during pre-occultation and post-occultation phase.

Parameters		Pre-occultation phase												Post-occultation phase								
date	[calender day]	Nov 06, 1968	Nov 07, 1968	Nov 08, 1968	Nov 09, 1968	Nov 10, 1968	Nov 11, 1968	Nov 12, 1968	Nov 13, 1968	Nov 14, 1968	Nov 15, 1968	Nov 16, 1968	Nov 17, 1968	Nov 29, 1968	Nov 30, 1968	Dec 01, 1968	Dec 02, 1968	Dec 03, 1968	Dec 04, 1968	Dec 05, 1968	Dec 06, 1968	Dec 07, 1968
x	[indexed day]	1	2	3	4	5	6	7	8	9	10	11	12	13	14	15	16	17	18	19	20	21
r_x	[R_S]	9.96	9.30	8.78	8.21	7.51	7.01	6.39	5.76	5.16	4.54	4.01	3.04	−4.20	−4.86	−5.49	−6.06	−6.72	−7.29	−7.98	−8.65	−9.29
χ	[Rs]	0.001	0.001	0.001	0.001	0.001	0.001	0.001	0.001	0.001	0.001	0.001	0.001	0.001	0.001	0.001	0.001	0.001	0.001	0.001	0.001	0.001

Continued

z R.M. Goldstein	z L. Accardi *et al.*	z P. Merat *et al.*	z A.Trinchera	Grav. z Earth	Grav. z Sun	z ntl tot (interactional z)	z ntl down	z ntl up	ce	ψ	max ne
[-]	[-]	[-]	[-]	[-]	[-]	[-]	[-]	[-]	[cells]	[-]	[el/m^3]
1.2E-08	2.0E-08	1.5E-08	1.5E-08	-6.96E-10	9.96E-09	5.7E-09	2.454E-09	3.293E-09	3	1	5.0E+09
1.3E-08	2.2E-08	1.7E-08	1.8E-08	-6.96E-10	9.96E-09	8.3E-09	3.764E-09	4.496E-09	6	2	6.5E+09
1.9E-08	2.4E-08	1.9E-08	1.8E-08	-6.96E-10	9.96E-09	9.2E-09	3.987E-09	5.168E-09	6	2	7.5E+09
2.9E-08	2.5E-08	2.1E-08	2.3E-08	-6.96E-10	9.96E-09	1.3E-08	5.411E-09	8.053E-09	9	3	9.0E+09
2.8E-08	2.7E-08	2.3E-08	2.2E-08	-6.96E-10	9.97E-09	1.3E-08	5.851E-09	7.037E-09	12	4	1.1E+10
3.2E-08	2.9E-08	2.4E-08	2.3E-08	-6.96E-10	9.97E-09	1.4E-08	6.415E-09	7.439E-09	15	5	1.3E+10
3.7E-08	3.2E-08	2.7E-08	2.6E-08	-6.96E-10	9.97E-09	1.7E-08	7.812E-09	9.252E-09	21	7	1.7E+10
3.4E-08	3.7E-08	3.1E-08	2.9E-08	-6.96E-10	9.97E-09	2.0E-08	9.169E-09	1.056E-08	30	10	2.2E+10
3.8E-08	4.1E-08	3.4E-08	3.5E-08	-6.96E-10	9.98E-09	2.6E-08	1.197E-08	1.391E-08	51	17	3.0E+10
4.2E-08	5.0E-08	3.9E-08	4.3E-08	-6.96E-10	9.98E-09	3.4E-08	1.4399E-08	1.9174E-08	78	26	4.1E+10
4.4E-08	6.0E-08	4.5E-08	4.5E-08	-6.96E-10	9.98E-09	3.6E-08	1.744E-08	1.83E-08	132	44	5.6E+10
4.9E-08	8.0E-08	6.2E-08	6.1E-08	-6.96E-10	9.98E-09	5.2E-08	2.639E-08	2.517E-08	318	106	1.1E+11
5.2E-08	5.3E-08	5.2E-08	5.4E-08	-6.96E-10	1.00E-08	4.4E-08	2.165E-08	2.267E-08	185	37	5.0E+10
4.8E-08	4.3E-08	4.5E-08	4.4E-08	-6.96E-10	1.00E-08	3.5E-08	1.693E-08	1.793E-08	105	21	3.5E+10
4.4E-08	3.8E-08	4.1E-08	3.5E-08	-6.96E-10	1.00E-08	2.6E-08	1.240E-08	1.337E-08	55	11	2.5E+10
4.2E-08	3.4E-08	3.6E-08	3.4E-08	-6.96E-10	1.00E-08	2.5E-08	1.133E-08	1.358E-08	40	8	2.0E+10
5.3E-08	2.9E-08	3.4E-08	3.4E-08	-6.96E-10	1.00E-08	2.5E-08	1.024E-08	1.47E-08	30	6	1.5E+10
2.9E-08	2.7E-08	3.2E-08	2.6E-08	-6.96E-10	1.00E-08	1.7E-08	7.854E-09	8.951E-09	20	4	1.2E+10
2.6E-08	2.5E-08	2.8E-08	2.4E-08	-6.96E-10	1.00E-08	1.5E-08	6.829E-09	7.905E-09	15	3	9.5E+09
2.5E-08	2.4E-08	2.7E-08	2.4E-08	-6.96E-10	1.00E-08	1.5E-08	6.956E-09	7.911E-09	15	3	7.9E+09
2.3E-08	2.3E-08	2.5E-08	2.2E-08	-6.96E-10	1.00E-08	1.2E-08	5.2268E-09	7.2474E-09	10	2	6.6E+09

From calculations, we can extract Figure 17 in which we trace the redshift trend based on the pure interactional redshift calculated. We can observe that:

- The total redshift increases reaching a peak before the occultation of the radio signal and then decreases once the occultation ceases. The greater the density of photo-ionized electrons through which the radio signal travels, the higher the probability of interacting with electrons on the path. Accordingly, the probability of losing energy in the process of absorption and re-emission of the signal is higher;
- The redshift in the upper part of the orbital model is slightly greater than the redshift in the lower part as the point of emission of the signal by the space probe is already in a place where the electron density is greater than the opposite position of the earth. In this optic, we observe the configuration symmetrically with respect to the Sun along the transition line dividing the upper part from the lower part;
- The redshift in the lower part appears to be more linear without major dips. As mentioned in the previous point, it is the greater distance from the Earth to the Sun, compared to the lower distance between Pioneer-6 and the Sun, that smoothens the redshift trend. In the upper part the electron densities are on average higher and the transition from a circular sector, having a specific calculated average electron density, is sudden and causes peaks in the curve.

However, the peaks in the curve are exactly what R.M. Goldstein detected with the graph of the variation of the central frequency over the days of measurement. Below, in Figure 18, we compare the curve of this study case based on the interactional redshift together with the contribution of the gravitational redshift and the curve of R.M. Goldstein [10] in terms of wavelength rather than frequency variation, according to the transcription of P. Merat *et al.* The other two graphs result from further publications, P. Merat *et al.* [11] and L. Accardi *et al.* [12], which trace an expected trend of the redshift curve based on their calculation methods. Only R.M. Goldstein's curve, as transcripted by P. Merat *et al.*, is to be considered a real trend for the redshift as it is based on pure observational data and not on a calculation method. As we can observe, the curve obtained from this study is also very close to the real observations except for external effects, such as solar flares, which affect the redshift.

Also in Figure 18, we can make important observations:

- The redshift trend obtained through this study varies along the nominal values achieved by P. Merat *et al.* (pre-occultation) and L. Accardi *et al.* (post-occultation). Close to the phase prior to and immediately subsequent to the occultation, the redshift values and the trend of the curves are almost identical;
- The oscillations of the curve in both pre-occultation and post-occultation phase are not calculation errors but represent the real trend of the curve, as firstly, there are no intermediate measurements between one day and the next, neither of the redshift nor of the orbital parameters, thus giving rise to

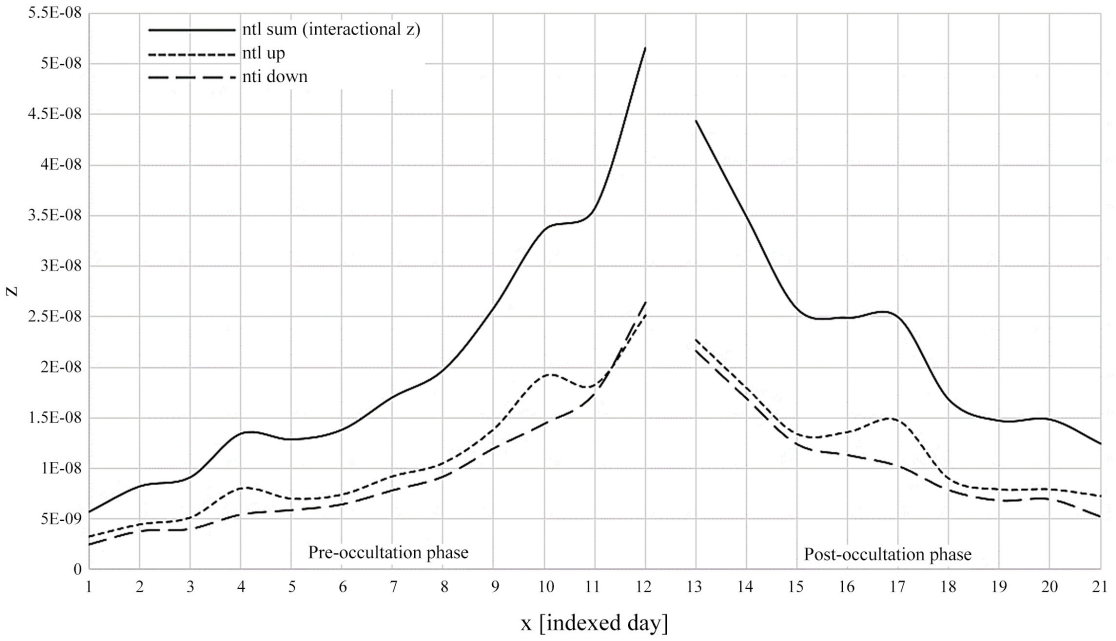

Figure 17. Total interactional redshift trend and its contribution over the measurement days.

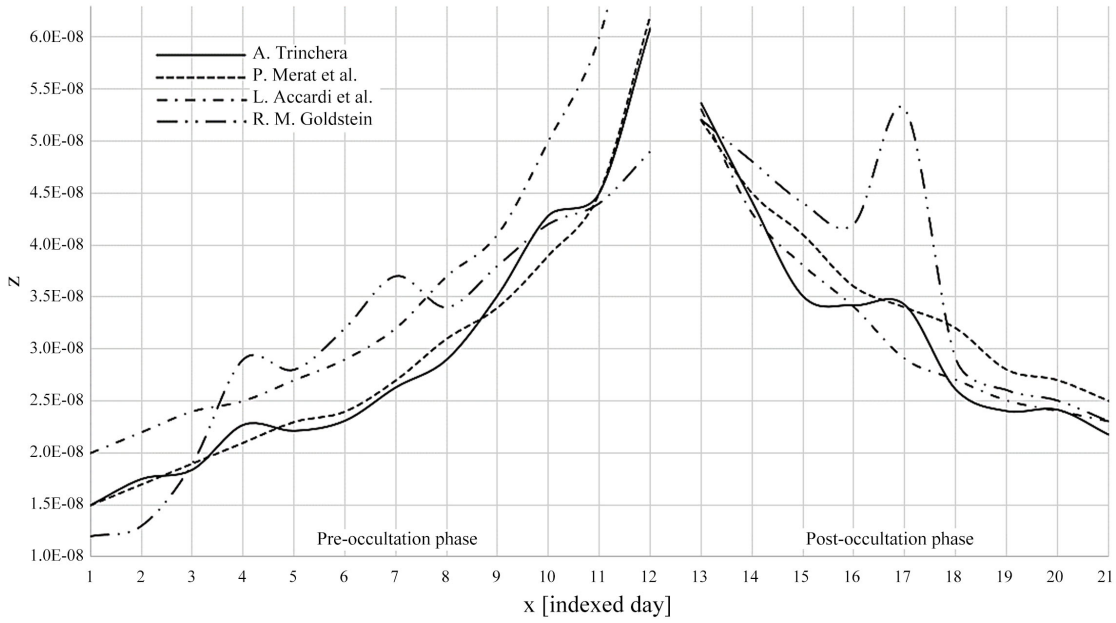

Figure 18. Total redshift and its comparison to other scientific studies.

slight jumps in the curve; secondly, the redshift trend is not purely described by a given power trend as the curve is the combination of a variation according to a certain power coming from the electron density together with the exponential variation of the interactional redshift dependent on geometric variations of the physical intervals and overall distances variable day by day. In short, the curve is a combination of physical parameters such as the variable distribution of electron density, the interactions between photons and electrons, and, last but not least, the geometric characteristics of the orbital

model of Earth and Pioneer-6;

- R.M. Goldstein's curve shows redshift values almost coinciding with the redshift values of the present study along the initial and final days of the pre-occultation and post-occultation phases. In the central phases, there appear to be amplifications of the curve with respect to the values obtained from the present study. In detail, the curve that we calculated seems to have the same peaks compared to R.M. Goldstein's curve. However, our peaks appear lower in intensity. The peaks are not random but describe exactly the geometry and physics of the redshift anomaly. The peaks of the R.M. Goldstein detections are amplified on average by a factor of about 2E-08 in terms of redshift. It is the amplification distributed over the entire time span of the measurements that is due to the solar flares and not due to the amplification on the peaks. This does not exclude the fact that, at the peaks in the post-occultation phase, being extremely high, a solar flare may have occurred. In support to this statement, there is a publication which indicates the presence of at least one solar flare which occurred during the measurements on 1968 December 3 [19];
- In this article, we have considered the gravitational redshift components of Sun and Earth at the point of reception of the radio signal, as they are also decisive for the final redshift calculation. On average, the sum of the two gravitational components increases the total redshift by a factor of 9E-09 being the interactional redshift of the order of 1E-08, as can be observed from the tables;
- The component of interactional redshift between the radio signal and the photo-ionized electrons is on average 2E-08 throughout the duration of the observation, going from a minimum of 6E-09 to a maximum of 5E-08;
- The redshift components linked to the rotation and to the orbital speeds of the Earth as well as to the Pioneer-6 space probe have not been included as they have been intrinsically removed from the terrestrial radio signal receiver due to its set-up. Accordingly, they have not been transferred into the redshift curves;
- Moreover, it is possible to state again that the Mex October 2006 electron distribution, referred to the solar corona, is the one that best represents the real physical electron distribution around the Sun [8].

8. Conclusions

The total redshift is a response between the interactional redshift, intended as NTL contributions to which we add up the gravitational redshift contributions of the Sun and the Earth, and the Mesh Approach as well as the Wigner-Crystal Precondition. The latter selects the electrons and consequently the number of contributions as well as the intensity of the redshift. The redshift trend obtained from this study, corresponds, less than the solar flares, to the redshift trend obtained from observational data. The theoretical basis used in our calculation method concerns the loss of energy of the radio signal, characterized by a specif-

ic wavelength, which travels through a variable medium dense with photo-ionized electrons. They absorb the incident photons and re-emit them with an imperceptibly wider wavelength. It is possible to sum the contributions of interactional redshift only starting from specific values of electron density and temperatures which satisfy the Wigner-Crystal Precondition of the crystals, centered in the electrons, for which their unitary potential energy is greater than their kinetic energy. The condition allows the radio signal, through the formation of the crystal, not to undergo deviations on the trajectory and not to detect, as expected in other scattering processes, any blurring phenomenon. Where the Wigner-Crystal Precondition is not verified, the scattering of radio photons with electrons is very likely and it is attributed to a Thomson scattering. We can state that the redshift of the radio signal of the Pioneer-6 space probe is real: measured by a terrestrial radio receiver and calculated in detail. The discovery made in this study on how and why the radio signal, under particular physical-mathematical conditions, undergoes a redshift, should not only be considered a local phenomenon, on a solar scale, but also a cosmic phenomenon on a larger scale applicable to all stars and galaxies as it is exclusively dependent on the distance of the astronomical object, on the density and temperature of the electrons in the surrounding environment and on the wavelength of the emitted signal.

9. Discussions

Similarly to the action that the Sun has in interstellar space, it is also possible to extend the same considerations and calculation methods of the interactional redshift on an intergalactic and extragalactic scale. Indeed, the galaxies, composed of stars, are surrounded by photo-ionized hydrogen that permeates the intergalactic space that is, in turn, crossed by photons of light. Once removed the Doppler contributions of proper and rotational motion of astronomical objects, the so-determined residual redshift is a contribution related to the density and temperature of the electrons as well as the physical properties of the electron, the distance travelled and the wavelength of the photons.

The term "anomalous" referred to redshift measurements which deviate from expectations is actually a key element for the understanding of the redshift mechanism. Moreover, the Hubble constant is considered as an energy loss parameter related to the electron density distribution through which photons travel. For this reason, it should not be surprising that the Hubble constant can assume several different values depending on the astronomical object in question, as electron-dense atmospheres vary, and on the length of the spatial direction under observation. This point has been fully argued in this study where, due to the solar scale under examination, a small value of the redshift has been detected not only by observational data, but it has been calculated with an analytical and numerical approach. It is always worth mentioning the fact that there are many cases described in the smallest detail of redshift inconsistencies, related to the current conception of redshift in the expansion model, where high-redshift Quasars are observed too close to low-redshift galaxies, connected in some cases

with bridges of matter [20], and in others cases they are even detected at the various wavelengths in front of companion galaxies [21].

Conflicts of Interest

The author declares no conflicts of interest regarding the publication of this paper.

References

[1] Ashmore, L.E. (2019) Calculating the Redshifts of Distant Galaxies from First Principles by the New Tired Light Theory (NTL). *Journal of Physics: Conference Series*, **1251**, Article ID: 012007. https://doi.org/10.1088/1742-6596/1251/1/012007

[2] Ashmore, L.E. (2016) An Explanation of Redshifts in a Static Universe. In: Amoroso, R.L., Kauffman, L.H. and Rowlands, P., Eds., *Unified Field Mechanics*, World Scientific Publishers, Singapore, 456-462.

[3] Ashmore, L.E. (2016) A Relationship Between Dispersion Measure and Redshift Derived in Terms of New Tired Light. *Journal of High Energy Physics, Gravitation and Cosmology*, **2**, 512-530. https://doi.org/10.4236/jhepgc.2016.24045

[4] Ashmore, L.E. (2006) Recoil between Photons and Electrons Leading to the Hubble Constant and CMB. *Galilean Electrodynamics*, **17**, 53-57.

[5] Ashmore, L.E. (2019) Galaxies "Boiling off" Electrons Due to the Photo-Electric Effect Leading to a New Model of the IGM and a Possible Mechanism for "Dark Matter". *Journal of High Energy Physics, Gravitation and Cosmology*, **5**, 181-192. https://doi.org/10.4236/jhepgc.2019.51010

[6] Zwicky, F. (1929) On the Red Shift of Spectral Lines through Interstellar Space. *Proceedings of the National Academy of Sciences of the United States of America*, **15**, 773-785. https://doi.org/10.1073/pnas.15.10.773

[7] Adam, M.G. (1948) Interferometric Measurements of Solar Wavelengths and an Investigation of the Einstein Gravitational Displacement. *Monthly Notices of the Royal Astronomical Society*, **108**, 446-464. https://doi.org/10.1093/mnras/108.6.446

[8] Trinchera, A. (2021) Redshift Anomaly on the Solar Disk as Multiple Interactions between Photons and Electrons. *Journal of High Energy Physics, Gravitation and Cosmology*, **7**, 1-51. https://doi.org/10.4236/jhepgc.2021.71001

[9] Verma, A.K., Fienga, A., Laskar, J., Issautier, K., Manche, H. and Gastineau, M. (2013) Electron Density Distribution and Solar Plasma Correction of Radio Signals Using MGS, MEX and VEX Spacecraft Navigation data and Its Application to Planetary Ephemerides. *Astronomy & Astrophysics*, **550**, Article No. A124. https://doi.org/10.1051/0004-6361/201219883

[10] Goldstein, R.M. (1969) Superior Conjunction of Pioneer 6. *Science*, **166**, 598-601. https://doi.org/10.1126/science.166.3905.598

[11] Merat, P., Pecker, J.C. and Vigier, J.P. (1974) Possible Interpretation of an Anomalous Redshift Observed on the 2292 MHz Line Emitted by Pioneer-6 in the Close Vicinity of the Solar Limb. *Astronomy & Astrophysics*, **30**, 167-174. http://adsabs.harvard.edu/full/1974A%26A....30..167M

[12] Accardi, L., Laio, A., Lu, Y.G. and Rizzi, G. (1995) A Third Hypothesis on the Origin of the Redshift: Application to the Pioneer 6 Data. *Physics Letters A*, **209**, 277-284. https://doi.org/10.1016/0375-9601(95)00868-3

[13] Parthasarathy, R., Hills, H.K., Couzens, D.A. and King, J.H. (1986) Trajectories of

Pioneers 6-11, Helios A and B, and Voyagers 1 and 2. https://omniweb.gsfc.nasa.gov/coho/helios/book1/b1_title.html

[14] Levy, G.S., Sato, T., Seidel, B.L., Stelzried, C.T., Ohlson, J.E. and Rusch, W.V.T. (1969) Pioneer 6: Measurement of Transient Faraday Rotation Phenomena Observed during Solar Occultation. *Science*, **166**, 596-598. https://doi.org/10.1126/science.166.3905.596

[15] Williams, R.E. (1965) The Size of a Solar H II Region. *Astrophysical Journal*, **142**, 314 p. https://doi.org/10.1086/148286

[16] Wigner, E.P. (1934) On the Interaction of Electrons in Metals. *Physical Review*, **46**, Article No. 1002. https://doi.org/10.1103/PhysRev.46.1002

[17] Wigner, E.P. (1938) Effects of the Electron Interaction on the Energy Levels of Electrons in Metals. *Transactions of the Faraday Society*, **34**, 678-685. https://doi.org/10.1039/tf9383400678

[18] Alexander, R.L., Gilbert, J.A., Landi, R., Simoni, M. and Zurbuchen, T.H. (2011) Audification as A Diagnostic Tool for Exploratory Heliospheric Data Analysis. *The 17th International Conference on Auditory Display*, Budapest, Hungary, 20-24 June 2011.

[19] Ferencz, C. and Tarcsai, G. (1974) Redshift during Pioneer-6 Solar Occultation Unexplained or Predicted. *Nature*, **252**, 615. https://doi.org/10.1038/252615a0

[20] Arp, H. (1987) Quasars, Redshifts and Controversies. Interstellar Media, Barkeley.

[21] Lopez-Corredoira, M. and Gutiérrez, C.M. (2004) The Field Surrounding NGC 7603: Cosmological or Non-Cosmological Redshifts? *Astronomy & Astrophysics*, **421**, 407-423. https://doi.org/10.1051/0004-6361:20034260

Appendix A

Planck constant h	6.626E−034	m^2kg/sec
Electron mass m_e	9.109E−031	kg
Electron radius r_e	2.818E−015	m
Electron charge e	1.602E−19	C
Light speed c	299792458	m/sec
Sun radius R_{sun}	695510000	m
Sun mass M_s	1.989E+030	kg
Gravitational constant G	6.674E−011	$m^3/kgsec^2$
Earth radius R_E	6371000	m
Earth mass M_E	5.972E+024	Kg
Astronomical unit AU	149.597E+09	m
Boltzmann constant k_B	1.38E−23	m^2kg/sec^2K
Free space permittivity ε_0	8.854E−12	F/m

Appendix B

All calculations of the spreadsheet, contained in Appendix B, are not fully reported as they would exceed the limit number of pages. All full data can be shared to any researcher on request.

Nov 06, 1968 (up)

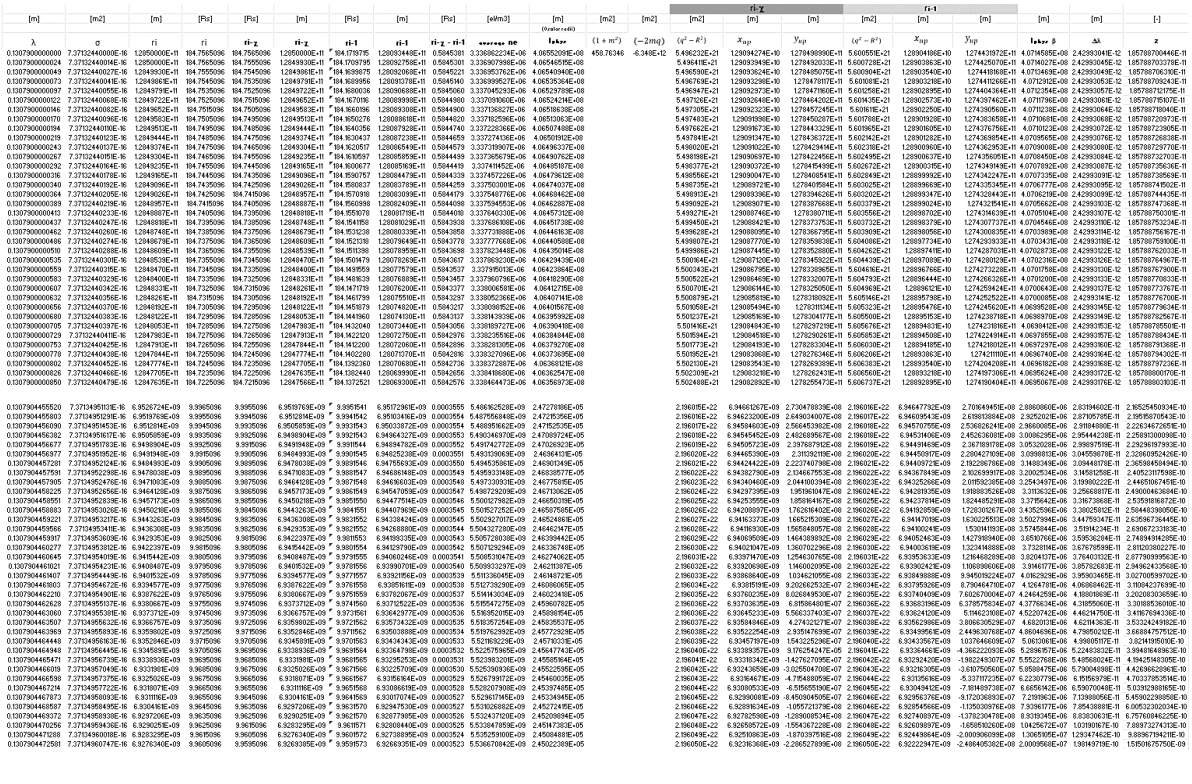

Nov 06, 1968 (down)

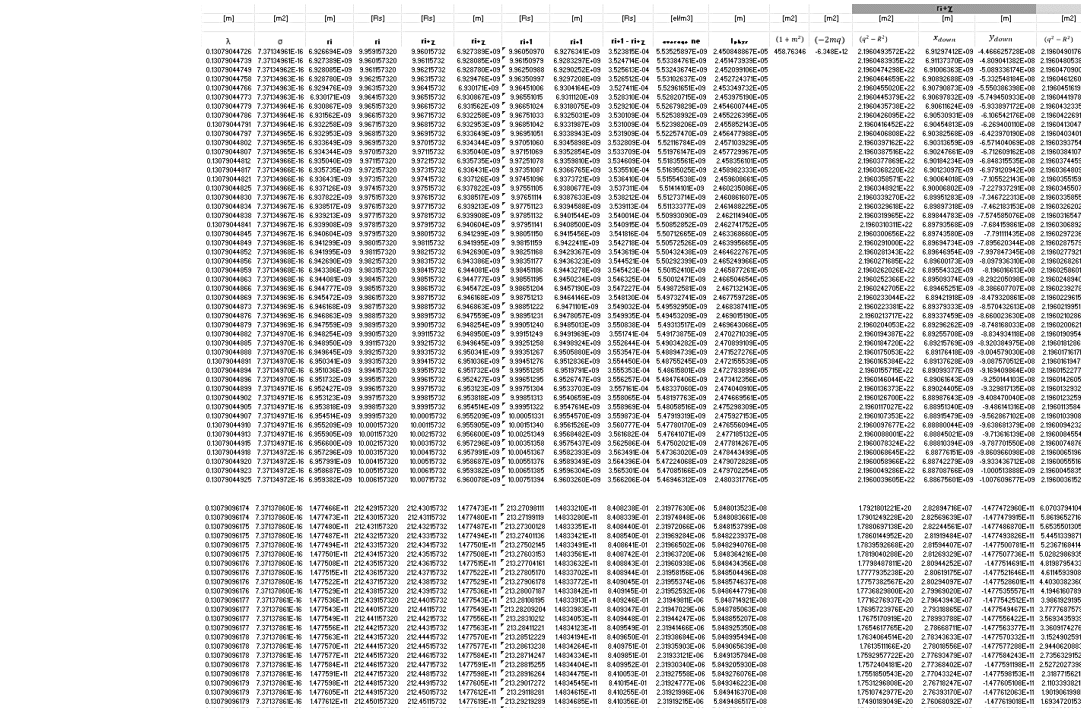

Nov 07, 1968 (up)

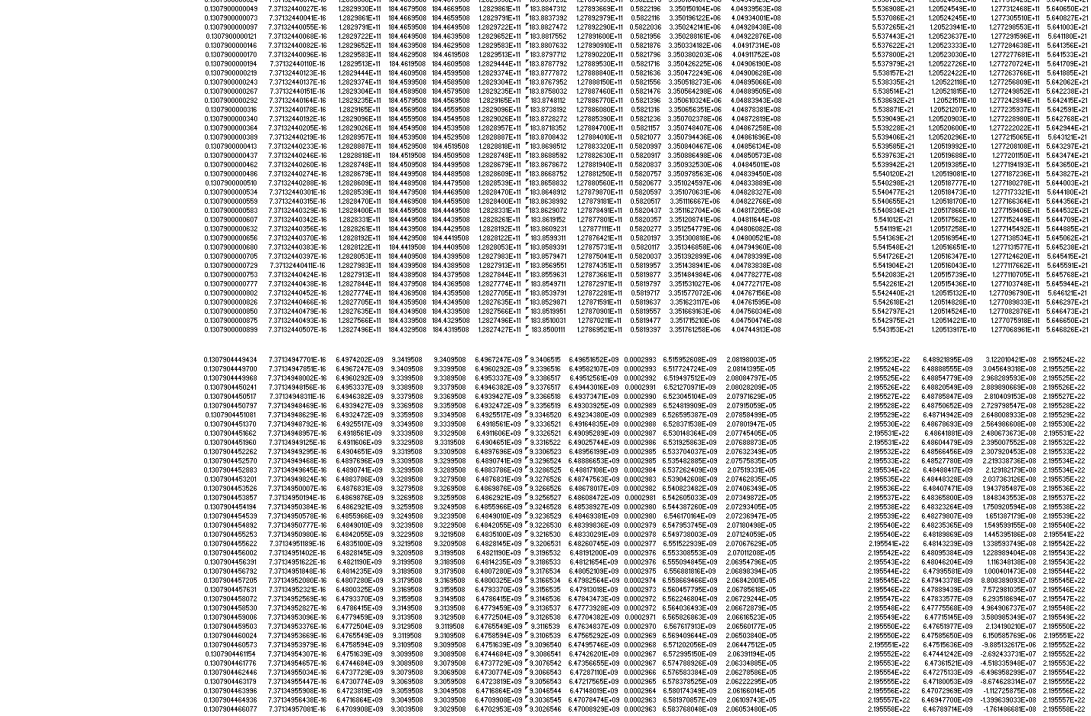

Nov 07, 1968 (down)

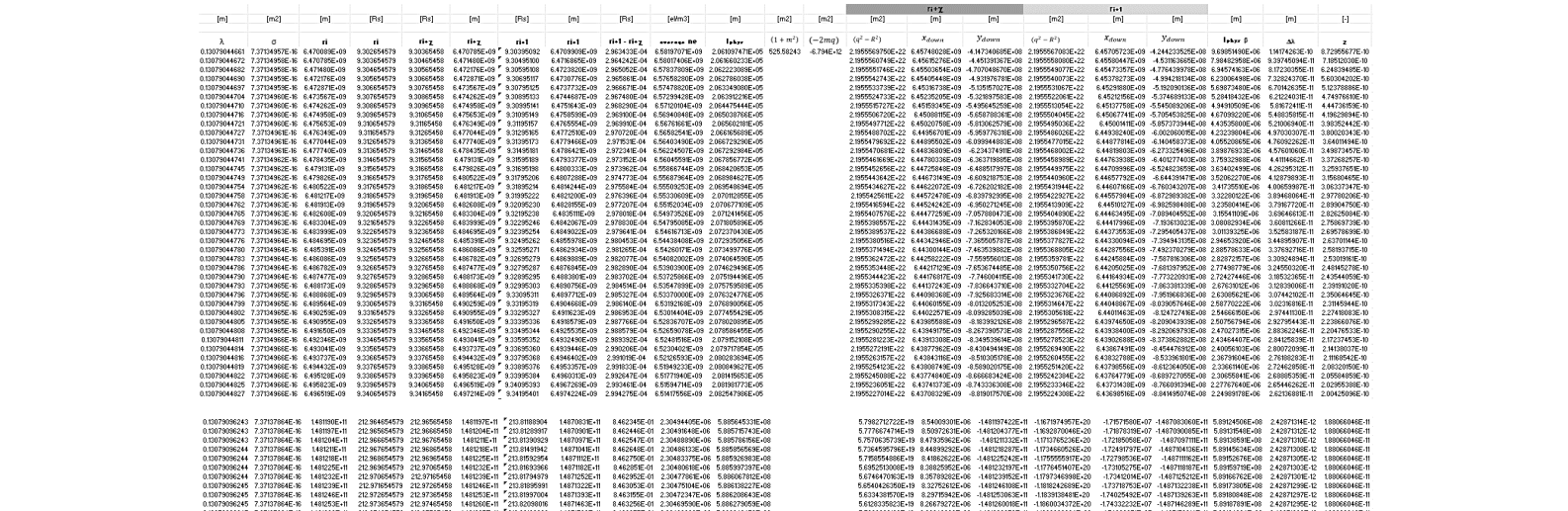

Nov 08, 1968 (up)